RSC Advances

PAPER

View Article Online
View Journal | View Issue

Cite this: *RSC Adv.*, 2026, **16**, 9054

Magnetic graphene-based ferrite nanoparticles: synthesis, characterization, and anti-proliferative activity against some human cancer cells (*in vitro* study)

Abdelsattar O. E. Abdelhalim, *[a] Nasra F. Abdel Fattah, [b] Mohamed Z. Hussein,[a] Mangoud M. Mangoud [a] and Samah A. Loutfy *[b]

This work introduces a novel soft magnetic building block (GCM), based on reduced graphene oxide covalently functionalized with Congo red molecules and incorporated with barium ferrite nanoparticles, creating a promising multifunctional platform for future magnetically controlled nanorobotic systems for potential cancer therapy and diagnosis nanodevices. The sol–gel auto-combustion method was used for the synthesis of pure barium ferrite (M) and *in situ* synthesis of reduced graphene oxide–barium ferrite nanoconjugate (GM). Physicochemical characterization techniques were used for identification, including infrared spectroscopy, X-ray diffraction, UV-visible spectroscopy, thermogravimetric analysis, scanning electron microscopy, energy-dispersive X-ray spectroscopy, high-resolution transmission electron microscopy, vibrating sample magnetometry, size distribution analysis, and ζ-potential analysis. M showed hard ferrimagnetic properties with a coercivity (H_c) of 2183 Oe, while GCM and GM demonstrated soft ferrimagnetic character with H_c values of 212 Oe and 147 Oe, respectively. Barium ferrite demonstrated higher saturation magnetization (M_s) than both GCM and GM. M_s values of 59 emu g^{-1}, 35 emu g^{-1}, and 25 emu g^{-1} were recorded for M, GCM, and GM, respectively. The decreased saturation magnetization is attributed to spin disorder due to the presence of graphene domains with defects and different functional groups on the GCM and GM surfaces. MTT assays revealed that the barium ferrite graphene derivatives (GM/GCM) exhibited potent antiproliferative activity against both human colon cancer (HCT116) and human breast cancer cells (MCF-7), without affecting normal cells, with an IC_{50} range of 22.5–37 μg mL^{-1}. DNA fragmentation assays indicated that the graphene surface attached to Congo red molecules (GC/GCM) has a high activity for inducing DNA damage. Further insights into the mechanism of the apoptotic effect revealed that apoptosis was exerted *via* the intrinsic caspase-dependent pathway. Additionally, Congo red functionalization (GCM) further improved targeting specificity without compromising safety. qRT-PCR analysis demonstrated the upregulation of caspase-3, Bax, and p53. At the same time, downregulation of Bcl-2 was observed, confirming the enhanced apoptotic pathways in both cancer cell lines. The results were further supported using *in silico* studies, which showed high-affinity binding to the CD45 protein, with the strongest docking score (−22.92 kcal mol^{-1}) for GC.

Received 20th January 2026
Accepted 26th January 2026

DOI: 10.1039/d6ra00520a

rsc.li/rsc-advances

1 Introduction

Graphene is one of the carbon-based nanomaterials; other allotropes include nanodiamonds, fullerenes, and carbon nanotubes.[1] Graphitic structures, such as graphite, graphene, graphene oxide (GO) and its reduced form (rGO), are composed of several layers, and the unique structure of graphene derivatives endows them with exceptional surface properties such as high electrical and thermal conductivity, high surface area, good mechanical strength, optical transparency, and electronic mobility.[2] Graphene-based nanomaterials are emerging in several fields, such as energy,[3] water disinfection,[4] water desalination,[5] optoelectronics,[6] and biomedical applications.[7]

Functionalization of graphene surfaces enhances physicochemical properties as well as homogeneous dispersion.[8] The graphene surface can be functionalized through covalent and noncovalent approaches, such as amidation, esterification, 1,3-dipolarcycloaddition, and halogenation, in addition to hydrogen bonding, π–π stacking interactions, and hydrophobic interactions.[9–11] GO contains different oxygen functional groups,

[a]*Environmental Research Department, Chemical and Biological Research Division, National Center for Social and Criminological Research (NCSCR), 4 Agouza, Giza, 11561, Egypt. E-mail: abdelsattarosama@yahoo.com; mohamedzakihussein8@gmail.com; Mangoud_online@yahoo.com*

[b]*Virology and Immunology Unit, Cancer Biology Department, National Cancer Institute (NCI), Cairo University, Fom El-Khalig, 11796, Cairo, Egypt. E-mail: samah.loutfy@nci.cu.edu.eg; nasra_fathy87@yahoo.com*

such as epoxy, hydroxyl, carboxyl, lactol, and carbonyl groups, and the highly oxidized surface of graphene leads to stable dispersions and antioxidant and biocompatible properties.[12] These characteristics qualified GO as a promising candidate for biomedical applications such as targeted drug delivery, biosensing, diagnostics, regenerative medicine, bioimaging, chemotherapeutics, gene therapy, and radiotherapy.[13]

Vinothini *et al.* demonstrated that the noncovalent functionalization of GO with doxorubicin and rose bengal through hydrophobic and π–π stacking interactions led to high anticancer activity, as evaluated using the LDH assay, against MCF-7 breast cancer cells when exposed to 525 nm laser light irradiation. The synergistic effect of the conjugation between GO and the doxorubicin in the presence of rose bengal and the photodynamic effect led to apoptotic cell death and higher anticancer activity in comparison with the free drug doxorubicin.[14] Haider *et al.* revealed that GO covalently functionalized with peptides exhibited high affinity to placenta-specific protein 1, which is overexpressed on colorectal cancer cells, and the cancer treatment effect of the nanoconjugate was demonstrated by decreasing the invasiveness of HCT-116 and HT-29 cancer cells by 62% and 38%, respectively and downregulating PLAC-1 expression by 33% and 53%, respectively.[15]

Ferrite nanoparticles are applied in biomedicine fields, including anticancer, as antimicrobial agents and nanosensors, and for drug delivery.[16] Kohzadi *et al.* reported that GO functionalized with superparamagnetic iron oxide nanoparticles (SPION) and polyethylene glycol showed 50% cancerous cell death against EJ138 human bladder carcinoma at 300 ppm concentration, while the nanoconjugate of SPION with chitosan led to SARSCoV-2 virus inhibition by 86%.[17]

Congo red molecules are known for their binding to β-sheet structures of amyloid protein aggregates or fibril proteins.[18,19] Congo red can bind to the amyloid-β (Aβ) proteins associated with Alzheimer's disease, and it can be intercalated into the β-sheet structure of Aβ fibrils. The bonding between amyloid-like proteins and Congo red molecules occurs through hydrogen bonds established between the two β strands of amyloid fibril proteins and the nitrogen atoms of Congo red molecules,[20] in addition to the interaction between the two SO_3^{-1} functional groups of Congo red molecules and two of the positively charged amino acid residues located on two different amyloid protein molecules.[21] Congo red is widely used as a histological dye to detect amyloid fibrils (including Aβ-derived amyloids) in brain tissue and *in vitro* amyloid-fibril preparations.[22] Howie *et al.* showed that numerous pathologists utilize Congo red to diagnose amyloidosis, asserting the prevailing view that Congo red-stained amyloid exhibits apple-green birefringence under polarized light, often referred to as apple-green dichroism.[23]

Santiago *et al.* reported that many cancer types are related to the accumulation of amyloid β inside tumors due to hyperproduction of amylogenic proteins; the researchers concluded that amyloid growth in glioma tumors is a part of the tumor's environment, linked to the glial origin glioma cells, intra- and extracellular walls of blood vessels, and adjacent astrocytic endfeet, and might be utilized as an antigen for glioma imaging, marking, as well as a target for the development of a new class of anti-tumor therapeutics.[24] At the same time, Nguyen *et al.* published a case report concerning a 60 year-old woman with a right breast lesion, wherein amyloid nodal deposits linked to calcifications were observed after biopsy analysis, Congo red detected β-amyloid, and a characteristic apple-green birefringence of the Congo red dye was observed under polarized light.[25]

Ano Bom *et al.* demonstrated that mutant p53, commonly found in 50% of cancers, may organize into amyloid oligomers and fibrils in breast cancer tissues and *in vitro* due to a prion-like aggregation of the misfolded protein, which could be inhibited as a targeted cancer therapy.[26]

Amyloid-like β-sheet aggregates of mutant p53 are found in cancer cells but are absent in normal cells. The well-known ability of Congo red to bind β-sheet-rich amyloid structures may facilitate selective recognition of these aggregates, potentially interfering with mutant p53 aggregation, restoring partial p53 transcriptional activity, and reducing tumor cell proliferation *in vitro*.[26–29] Soragni *et al.* showed that amyloid-binding molecules can partially inhibit mutant p53 aggregation, reduce cytotoxic aggregates, and, in some contexts, restore partial p53 function.[30]

Zhao *et al.* demonstrated the effect of chemodynamic therapy caused by the magnetic carbon-coated $NiFe_2O_4$ nanocatalyst ferrites that can catalyze Fenton-like reactions in tumor microenvironments rich with H_2O_2, generating hydroxyl radicals that could intensify Fenton reaction activity and kill cancer cells.[31]

In this research, for the first time, covalent conjugation of the graphene surface with Congo red molecules was conducted with subsequent incorporation of barium ferrite nanoparticles. The produced rGO–Congo red–barium ferrite nanomaterial (GCM) was characterized using different techniques and compared with rGO–barium ferrite nanocomposite (GM), covalently conjugated graphene oxide-Congo red (GC), and pure compounds of graphene oxide (GO) and barium ferrite nanoparticles (M). The synthesized nanomaterials were characterized with several physicochemical methods such as infrared spectroscopy (IR), X-ray diffraction (XRD), UV-visible spectroscopy, thermogravimetric analysis (TGA), scanning electron microscopy (SEM) with energy-dispersive X-ray spectroscopy (EDX), high-resolution transmission electron microscopy (HRTEM), vibrating sample magnetometry (VSM), size distribution analysis, and ζ-potential analysis. The MTT assay was used to study the cytotoxicity of the nanomaterials against human colon cancer cells (HCT116) and human breast cancer cells (MCF-7). Moreover, DNA fragmentation assays were used to study the effect of the nanomaterials on the DNA content of the cancer cells. At the same time, the mechanism of the apoptotic pathway was investigated on a transcriptional level for some apoptotic gene expressions. In addition, the nanomaterials were tested for their biocompatibility on Vero cells (monkey kidney cells) as an *in vitro* model of normal cell control. Moreover, an *in silico* study was conducted to examine the molecular docking of the graphene structures on the cancer cells and explore the molecular mechanism underlying the observed apoptotic effect in our *in vitro* studies.

2 Materials and equipment

2.1 Reagents

To carry out the synthesis of graphene derivatives, the following reagents were used: graphite powder, sulfuric acid, sodium nitrate, potassium permanganate, deionized water, hydrochloric acid, hydrogen peroxide, distilled water, 1-ethyl-3-(3-dimethylaminopropyl) carbodiimide (EDC), *N*-hydroxysuccinimide (NHS), Congo red dye, sodium hydroxide, barium nitrate, iron nitrate nonahydrate, citric acid, ammonia solution 30%. All chemicals were of analytical grade and used without further purification.

Cells were maintained in Dulbecco's Modified Eagle Medium (DMEM), which was purchased from Sigma, Munich, Germany. This medium was supplemented with fetal bovine serum (10%), L-glutamine (1%), penicillin–streptomycin 100 IU per mL (1%) and sodium bicarbonate (3%) purchased from Gibco, Merelbeke, Belgium. Phosphate Buffer Saline (PBS) tablets and Trypsin–EDTA were obtained from Thermo Fisher Scientific, Loughborough, UK. 3-(4,5-Dimethylthiazol-2-yl)-2,5-diphenyltetrazoliumbromide (MTT) was purchased from Serva, Heidelberg, Germany. The qPCR SYBR Green Kit was obtained from Thermo-USA.

Cell lines: Vero cells were purchased from Vaccination and Sera Collection Organization (VACSERA), and the human cancer cells HCT116 and MCF-7 were purchased from Nawah company, Cairo, Egypt.

Molecular docking of Congo red and the graphene-based nanostructures was conducted using the Molecular Operating Environment (MOE) software,[32] a comprehensive molecular modeling platform widely recognized for its robust tools in protein–ligand docking, scoring, and visualization. The software's MMFF94X and AMBER10:EHT forcefields were used for ligand and receptor energy minimization, ensuring accurate simulation of molecular interactions within the active-site pocket.

2.2 Characterization equipment

The synthesized nanomaterials were identified using the following techniques: The functional groups in the synthesized nanomaterials were characterized using a Fourier-transform infrared (FTIR) spectrometer (a PerkinElmer Spectrum 65) within the wavenumber of 400–4000 cm^{-1}. Thermal stability was investigated using a thermogravimetric analyzer (LabSys Evo TGA) with a rate of 10 C min^{-1} under nitrogen atmosphere from room temperature to 600 °C. The magnetic properties, including hysteresis curves, saturation magnetization, and coercive field, were estimated using a vibrating sample magnetometer (VSM, Model: MSE-EZ9, Microsense, Lowell, MA, USA) device in a 1.5 tesla field at room temperature.

Morphology study was conducted using a field-emission scanning electron microscope (FE-SEM) (ZEISS-EVO 15) with energy-dispersive X-ray analysis (EDX) for surface imaging and elemental information, in addition to the high-resolution transmission electron microscopy (HRTEM) (JEM 2100 HRT, Japan), with an accelerating voltage of 200 kV and 0.2 nm resolution.

The crystal structure was recorded using X-ray diffraction (Brucker D8 Discover, Germany) with an X-ray wavelength of CuKα = 0.15140 nm. Ultraviolet-visible (UV/Vis) spectra were measured using a JENWAY 6850 UV/Vis spectrophotometer (England). The size distribution and ζ-potentials of the nanoparticles were measured using a Malvern Zetasizer 3000.

3 Synthesis methods

3.1 Synthesis of GO

GO (Fig. 1) was synthesized from graphite *via* a modified Hummers and Offeman oxidation method. Graphite powder (8 g) was dispersed in sulfuric acid (250 mL) in an ice bath and stirred for 20 min. $KMnO_4$ (16 g) was then added slowly with stirring for 25 min, followed by the addition of $NaNO_3$ (4 g) with continuous stirring for 2 h at a temperature below 5 °C. The temperature was gradually increased up to 45 °C for 1 hour. The reaction mixture was then stirred slowly while adding 250 mL of deionized water, and the temperature was elevated to 98 °C for 2 h, followed by adding 450 mL of deionized water and then 15 mL of 30% H_2O_2 to complete the oxidation process and remove excess $KMnO_4$. The GO residue was separated using filtration and washed repeatedly with deionized water and 5% HCl until reaching a neutral pH value for the GO precipitate, redispersed in deionized water, ultrasonicated for 1 h, and finally dried at 65 °C for 8 h.[33]

3.2 Synthesis of graphene oxide functionalized with Congo red molecules (GC)

GO powder (1 g) was dispersed in deionized water and ultrasonicated for 15 min, 0.3 g of EDC and 0.223 g of NHS were added gradually with continuous stirring for 2 hours, and then the pH of the mixture was raised to a slightly basic medium (pH 8) through the addition of 0.1 M NaOH with the subsequent addition of 0.135 g of Congo red dye dissolved in deionized water. The mixture was then stirred in a dark system for 24 hours, filtered, washed with deionized water several times until it reached neutral pH, and separated for drying in a vacuum for 6 hours. The structure of GC is shown in Fig. 2.

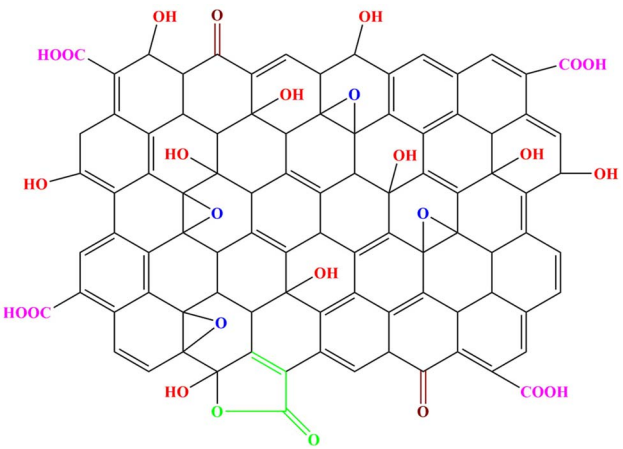

Fig. 1 Proposed structure of the GO nanomaterial.[33]

3.3 Synthesis of barium ferrite magnetic nanoparticles (M)

Barium ferrite was synthesized using the citrate sol–gel auto-combustion method.[34] Barium nitrate (0.002 mol) and iron nitrate nonahydrate (0.024 mol) were dissolved in 100 mL of deionized water, with the subsequent addition of 0.04 mol of citric acid dissolved in the minimum amount of deionized water. The solutions were stirred using a magnetic stirrer at room temperature for 30 minutes, and ammonia solution was added to get an alkaline medium with a pH value of 9. The mixture was stirred using a magnetic stirrer and heated at 80 °C until the transparent solution was converted into a viscous brown gel with foaming. The temperature was then maintained at 180 °C until the self-ignition process, which formed a loose powder that was completely crushed and milled. The ground powder was then calcined at 900 °C for 3 hours to form barium ferrite magnetic nanoparticles, $BaFe_{12}O_{19}$.

3.4 Synthesis of reduced graphene oxide functionalized with Congo red molecules and barium ferrite nanoparticles (GCM)

GC and M powders were mixed in a 1 : 1 weight ratio, crushed, milled, and dispersed in deionized water. The mixture was ultrasonicated for 20 minutes, then stirred for 5 hours at 140 °C. The dispersion was allowed to settle to remove excess water, heated to 250 °C in an oven, and finally filtered, dried at 70 °C, and ground to give the GCM powder (Fig. 3).

3.5 Synthesis of reduced graphene oxide functionalized with barium ferrite nanoparticles (GM)

GO powder (0.3 g) was dispersed in 100 mL of deionized water and ultrasonicated for 15 minutes, a mixture of barium nitrate (0.002 mol), iron nitrate nonahydrate (0.024 mol), and citric acid (0.05 mol) was dissolved in deionized water and added to the GO dispersion, with continuous stirring using a magnetic stirrer at room temperature for 30 minutes. The pH of the mixture was elevated to 9 to obtain an alkaline medium using ammonia solution, which was then stirred continuously during heating at 90 °C until a viscous and foamy gel was obtained. The temperature was raised to 190 °C to complete the auto-combustion reaction. A loose powder was formed, which was fully ground and sintered at 950 °C for 3 hours (Fig. 4).

4 *In vitro* study

4.1 MTT assay

The cytotoxic effect of the studied materials was assessed against the proliferation of human colon cancer cells (HCT116) and human breast cancer cells (MCF-7) using an MTT

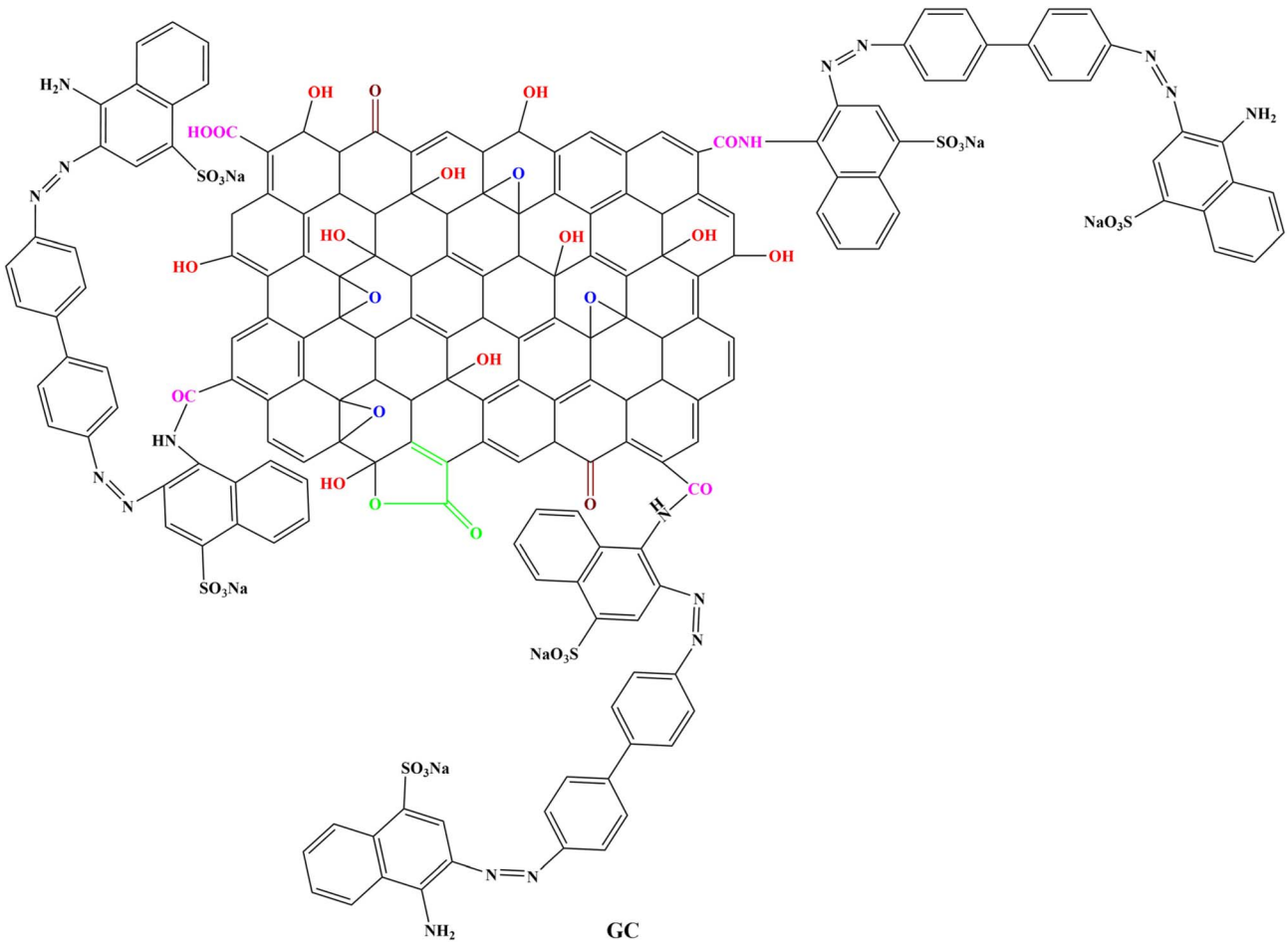

Fig. 2 Proposed structure of the graphene oxide functionalized with Congo red molecules (GC).

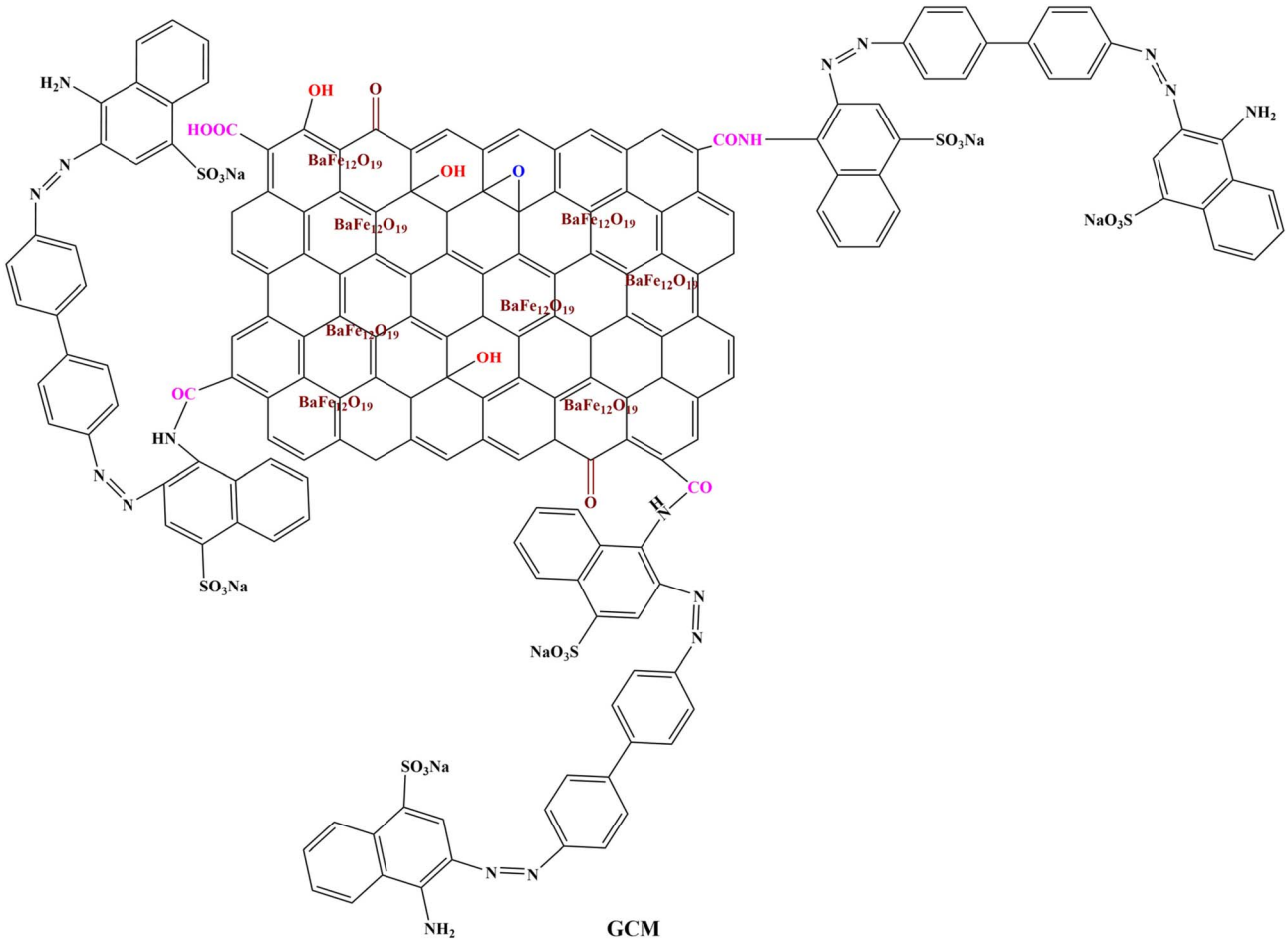

Fig. 3 Proposed structure of the reduced graphene oxide functionalized with Congo red molecules and barium ferrite nanoparticles (GCM).

colorimetric assay. Moreover, all compounds were tested on Vero cells (monkey kidney cells) as a model of normal control to evaluate their anti-proliferative activity towards non-cancerous cells.[35]

The assay relies on the reduction of tetrazolium salts into their insoluble formazan crystals that can be solubilized and measured spectrophotometrically.[36] First, the cells were seeded into a 96-well plate with a density of 104 cells per well and incubated overnight at 37 °C with 5% CO_2. The following day, the cells were treated with serial dilutions of all compounds separately. After 48 hours of incubation, 30 μL of 5 mg mL^{-1} MTT was added to each well and then incubated at 37 °C for 3 hours. The media was carefully removed, and 200 μL of dimethyl sulfoxide was added to each well to dissolve the insoluble formazan crystals. The absorbance was read at 570 nm using a multimode microplate reader (CLARIO star Plus, BMG LABTECH, Germany). The IC_{50} was calculated using non-linear regression analysis (log(inhibitor) *vs.* normalized response–variable slope) with GraphPad Prism software version 9.[37]

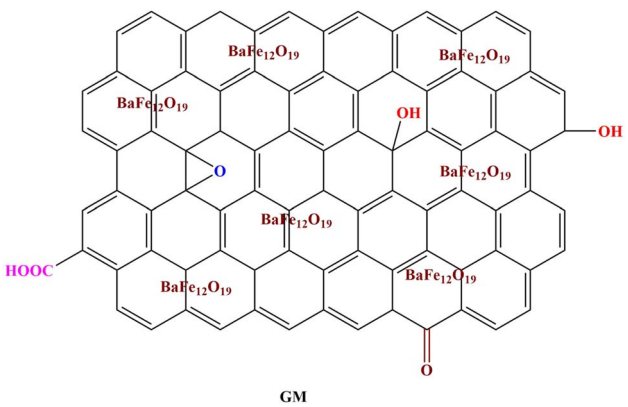

Fig. 4 Proposed structure of the reduced graphene oxide functionalized with barium ferrite nanoparticles (GM).

4.2 Morphological examination

Morphological changes were assessed after treatment of all the cells with the tested materials for 48 h, using an inverted microscope to confirm MTT results.

4.3 DNA fragmentation

Fragmentation of cellular DNA was investigated following individual treatment of the HCT116 cells with the IC_{50} of the tested materials in parallel with untreated cells (control) and incubated for 24 h. A fixed amount (350 ng) of cellular DNA extracted from treated and untreated cells using a Genomic

DNA Purification Kit (Amersham Biosciences) was subjected to 1.5% agarose gel electrophoresis in Tris–acetate buffer pH 8.2, and stained with 0.5 μg mL^{-1} ethidium bromide. The bands were examined under UV transillumination. Smearing, or the presence of many low molecular weight DNA fragments, is a characteristic feature of apoptotic cells.[38]

4.4 Effect of the tested materials on the expression of some apoptotic genes on a transcriptional level

4.4.1. Nucleic acid extraction. A Gene Jet RNA purification kit (Thermo Scientific, Inc, USA) was used for total RNA extraction according to the manufacturer's instructions, as used in our previous study. First-strand cDNA was synthesized using oligodT primers and the RevertAid Reverse Transcriptase kit (Thermo Scientific, USA).

4.4.2. Quantitative real-time PCR. Quantitative PCR (Q-PCR) was performed by using 12.5 μL SYBR Green reagent (Thermo Scientific, USA), 2 μL of synthesized cDNA, 3 μL of each primer of caspase-3, BCL2, BAX, and P53 genes, and β-actin, a housekeeping gene, was used as an internal control, and 4.5 μL of molecular-grade water in a total volume of 25 μL. Q-PCR was run in a quantitative real-time detection system (Applied Biosystems 7500 Fast Real-Time PCR system Thermal Cycling Block, USA). Amplification was performed under the following conditions: 1 minute at 95 °C, 40 cycles of 95 °C for 1 minute and 58 °C for 1 minute and 72 °C for 2 minutes. Post-amplification melting temperature (T_m) analysis clearly differentiated nonspecific PCR products. Negative controls (non-template water instead of cDNA) were also included to confirm the lack of reagent DNA contamination.

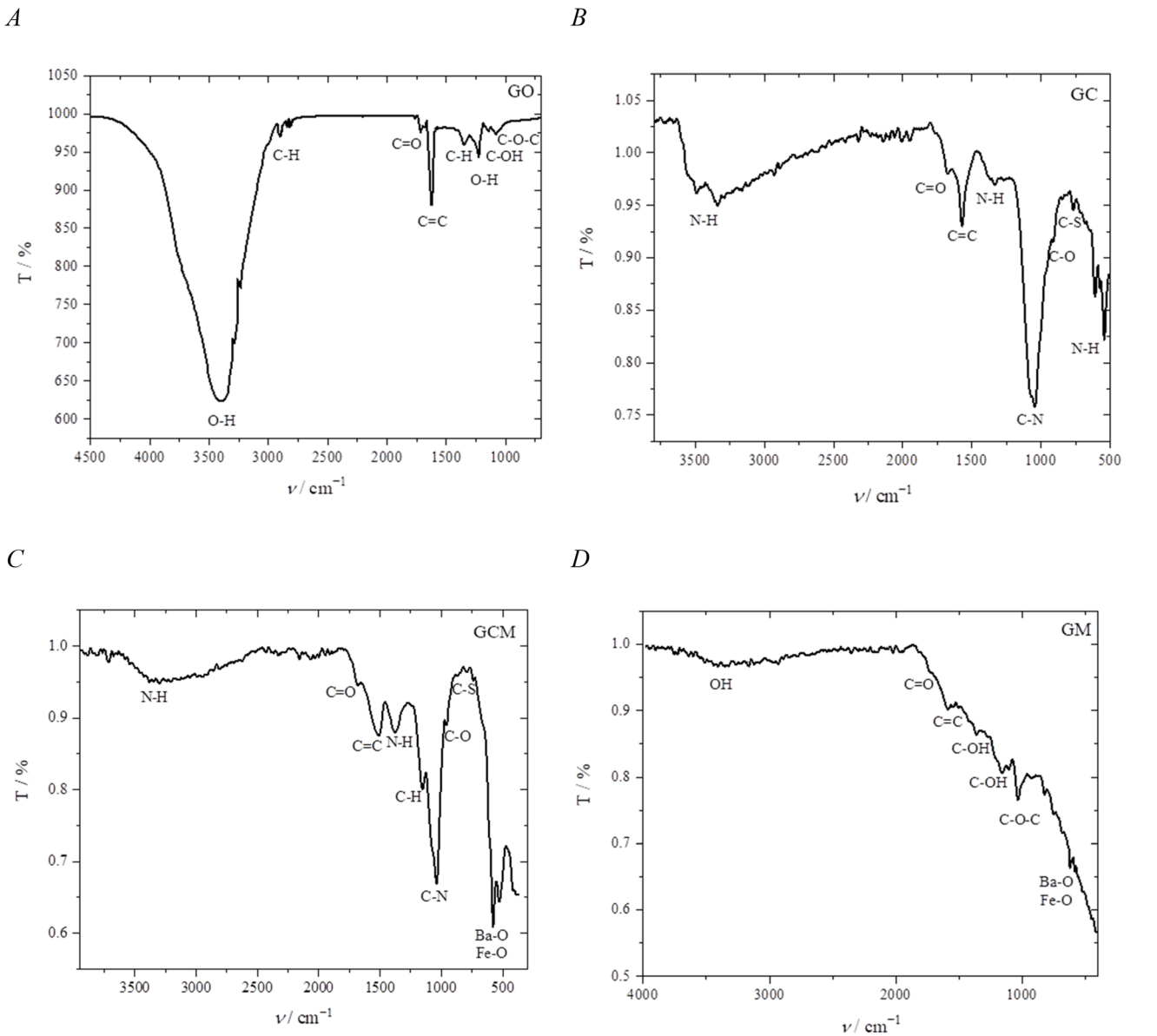

Fig. 5 IR spectra of GO (A), GC (B), GCM (C), and GM (D).

The Q-PCR data were analyzed using the comparative *CT* method. Briefly, the difference in cycle threshold, Δ*CT*, was determined as the difference between the tested gene and human β-actin. We then obtained ΔΔ*CT* by finding the difference between the two groups. The fold change (FC) was calculated as $2^{-\Delta\Delta CT}$.[39]

5 *In silico* study

5.1 Computational environment and software

Molecular docking studies were performed using the Molecular Operating Environment (MOE) software package, version 2008.10 (Chemical Computing Group, Montreal, Canada). All computational procedures, including ligand preparation, protein refinement, conformational analysis, and docking simulations, were carried out on a workstation running the Windows 10 operating system, ensuring consistent and reproducible performance throughout the workflow.

5.2 Choosing a docking target

Selecting an appropriate docking target is one of the most critical steps in obtaining meaningful, reliable, and biologically relevant molecular docking results. Yet, this task is often challenging for medicinal chemists due to the vast number of potential protein targets and the complexity of biological systems. To address this, computational target prediction tools such as TargetNet[40] provide valuable guidance. TargetNet is an open-access web server designed to predict the binding spectrum of small molecules by simultaneously generating a vast number of QSAR models derived from extensive chemogenomic datasets. Upon submission of a compound, the platform evaluates its potential interactions across 623 human proteins, producing a comprehensive drug–target interaction profile that can serve as a powerful decision-making tool in selecting a biologically plausible docking target.[41] In the present study, the SMILES notation of the sodium-free Congo red molecule was submitted to the TargetNet platform using default parameters present on the web page to identify the most probable protein targets for subsequent molecular docking analysis.

5.3 Target protein retrieval and preparation

The three-dimensional crystal structure of the target protein was downloaded from the Protein Data Bank.[42] This structure should include a selective co-crystallized ligand, allowing the use of the crystallographic ligand for docking protocol validation. After importing the structure into MOE, the protein structure was prepared through the following steps.

5.3.1. Initial structure inspection. The structure was checked for chain completeness, missing residues, steric clashes, and unnatural geometries.

5.3.2. Protonation and charge assignment. Protonation states of amino acid residues were assigned using the Protonate-3D tool. Partial atomic charges were then assigned automatically.

5.3.3. Duplicates, solvent and ion removal. Duplicates, crystallographic water molecules, sodium and sulphate ions were removed to avoid interference during docking.

5.3.4. Energy minimization. The cleaned protein structure was energy-minimized using the Amber10:EHT hybrid force field, which combines AMBER parameters for biomolecules and Extended Hückel Theory (EHT) for small molecules.[43] Minimization was performed with default convergence criteria to relieve steric strain while maintaining native binding-site geometry.

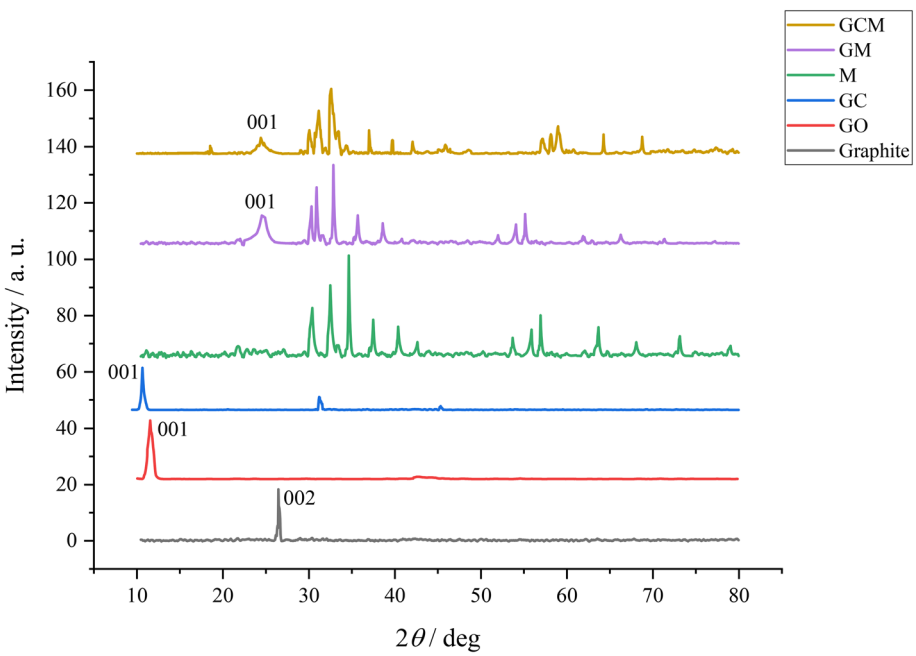

Fig. 6 XRD spectra of GO, GC, GCM, GM, and M.

5.4 Ligand construction and preparation

Ligand preparation included the depiction of a small representative structure for rGO, sodium-free Congo red, and a small representative sector of GC structure on MOE. All ligands were protonated and assigned partial charges in MOE, followed by energy minimization using the MMFF94X force field, which is well-suited to optimizing organic molecules and nanoscale carbon-based structures.[44] This process ensured that all ligand geometries were energetically stable prior to docking.

5.5 Docking protocol validation

To validate the docking protocol, the native co-crystallized ligand present in the downloaded protein structure was extracted and re-docked into the active site. Conformers of the ligand were generated through systematic rotation around rotatable bonds. The Triangle Matcher algorithm was used to place the ligand within the binding pocket, and initial poses were scored using the London dG scoring function. The highest-ranking poses were then refined by energy minimization inside

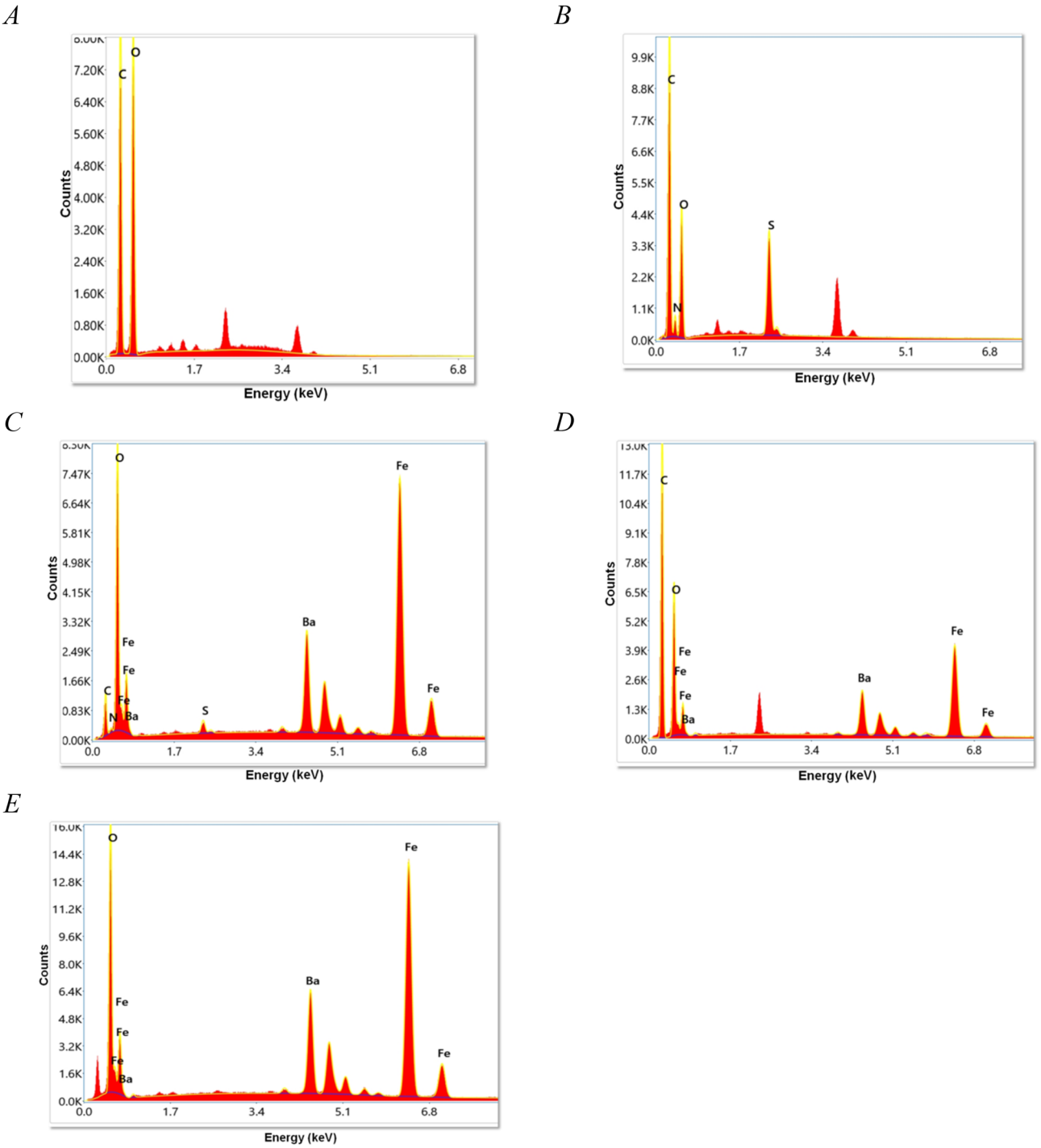

Fig. 7 EDX analysis of GO (A), GC (B), GCM (C), GM (D), and M (E).

the active site and subsequently re-scored. Agreement between the re-docked pose and the crystallographic conformation was assessed to ensure that the docking method could reliably reproduce experimentally observed intermolecular interactions.

5.6 Docking of prepared ligands

Following method validation, docking simulations for Congo red and graphene structures were performed using the same computational protocol. For each ligand, multiple conformations were generated and screened for optimal interaction with the active site of the target protein. Binding poses were prioritized based on predicted binding free energies and favorable electrostatic, hydrophobic, and hydrogen-bonding interactions with key residues in the catalytic pocket. The top-scoring poses were selected for further evaluation. Visualization of ligand–protein interactions was conducted within MOE to analyze hydrogen bonding, hydrophobic contacts, π–π stacking, and steric complementarity, providing a structural basis for interpreting the affinity and binding behavior of each ligand toward the target protein.

6 Results and discussions

6.1 Characterization of the nanomaterials

6.1.1. Infrared spectroscopy. Fig. 5 shows the IR spectra of GO (A), GC (B), GCM (C), and GM (D). In the GO spectrum, the broad peak at around 3400 cm^{-1} and the peak at about 1918 cm^{-1} are attributed to the O–H and C=O stretches of the carboxylic groups, respectively. The two peaks at 2900 cm^{-1} and 2825 cm^{-1} are related to the C–H stretches, while the two peaks around 1345 cm^{-1} and 1228 cm^{-1} are ascribed to the C–H and O–H bends, respectively. At the same time, the two peaks at 1136 cm^{-1} and 1080 cm^{-1} are assigned to the stretches of the C–OH phenolic and C–O–C epoxy groups, respectively. In the GC spectrum, the two peaks with spikes at around 3490 cm^{-1} and 3344 cm^{-1} are attributed to the N–H stretches of the amine and amide groups of Congo red molecules due to amidation reaction with the GO surface; at the same time, the peak located at 1680 cm^{-1} represents the C=O stretch of the amide groups. The peaks around 1335 cm^{-1}, 610 cm^{-1}, and 546 cm^{-1} are assigned to the N–H bends of the amide and amine groups, with the C–N stretch at about 1060 cm^{-1} and the C–S stretch of the Congo red molecules at 771 cm^{-1}. The peak around 1572 cm^{-1} is characterized as the C=C stretch of the aromatic domains, while the peak present at 916 cm^{-1} is specific for the C–O stretch of the hydroxyl and epoxy groups on the graphene surface.

In the GCM spectrum, the broad peak at 3321 cm^{-1} and the peak at 1688 cm^{-1} are attributed to the N–H and C=O stretches of the amide groups of the Congo red molecules; the amide group was shifted to slightly higher values due to the functionalization with barium ferrite nanoparticles. At the same time, the peaks located at 796 cm^{-1}, 1040 cm^{-1}, and 1379 cm^{-1} are related to the stretching frequencies of C–S, C–N, and N–H bonds of the Congo red molecule conjugated with the graphene surface, respectively. The two peaks at 957 cm^{-1} and 1158 cm^{-1} correspond to functional groups with C–O stretch and C–H bend on the GCM surface, while the peak around 1515 cm^{-1} is assigned to the aromatic domains, and the two peaks at 577 cm^{-1} and 529 cm^{-1} are related to the Ba–O and Fe–O bonds of the barium ferrite nanoparticles.[45] In the GM spectrum, the broad peak with low intensity at 3374 cm^{-1}, which is assigned to O–H stretch, reveals that the O–H bonds were reduced. Importantly, the appearance of the peak around 1739 cm^{-1} is attributed to the C=O stretching of the remaining carbonyl groups.

The C=C stretches of the aromatic domains appear at 1593 cm^{-1}. The two peaks at about 626 cm^{-1} and 590 cm^{-1} are attributed to the Ba–O and Fe–O bonds of the barium ferrite nanoparticles,[46] while the other bonds remaining on the graphene surface are characterized through the appearance of the following peaks: 1593 cm^{-1} (aromatic domains), 1374 cm^{-1} (C–OH carboxylic groups), 1165 cm^{-1} (C–OH phenolic groups), and 1030 cm^{-1} (epoxy groups). It is observed that the oxygen functional groups on the GO surface are reduced after the formation

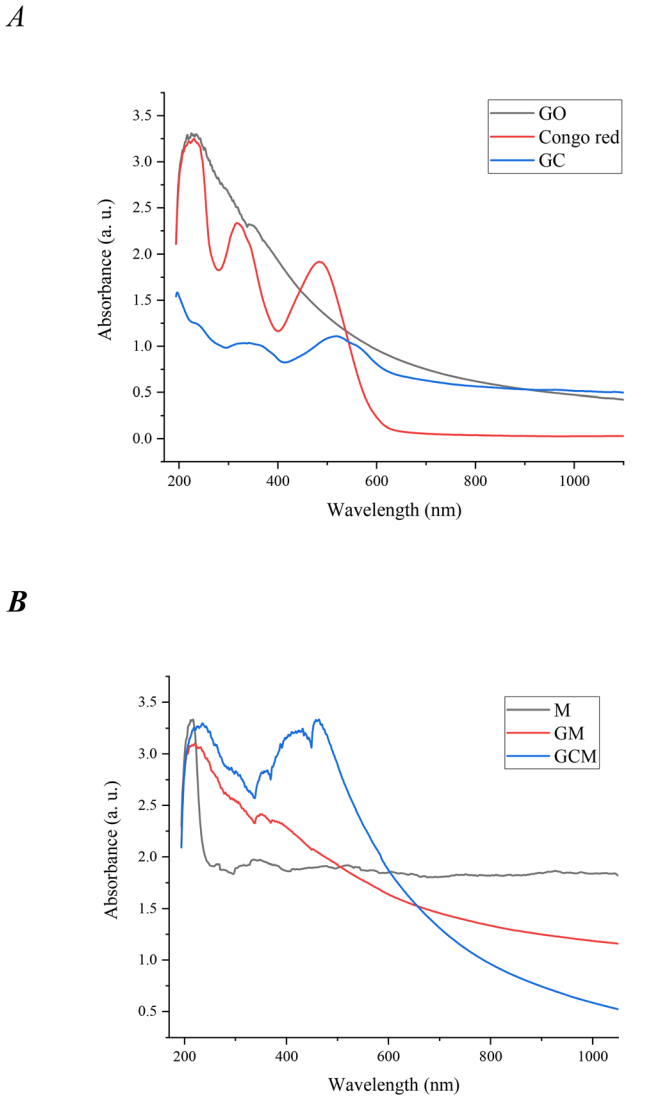

Fig. 8 UV-Vis spectra of GO, Congo red, and GC (A), and M, GM, and GCM (B).

of GCM and GM nanoparticles due to the synthesis conditions; this is confirmed by the decrease in intensity of the broad peak around 3400 cm^{-1}.[47,48]

6.1.2. X-ray diffraction. Fig. 6 demonstrates the XRD spectra of GO, GC, GCM, GM, and M. The peak at $2\theta = 26.5°$ is specific to the 002 plane of graphite, while, after oxidation, it shifted to $2\theta = 11.5°$, characteristic of the 001 plane of GO, confirming the oxidation of the graphite to GO. After the amidation reaction with Congo red molecules, the 001 plane of the GO was shifted to lower values at $2\theta = 10.6°$ in GC due to an increase in the interlayer distances after the conjugation, in addition to the appearance of another peak around $2\theta = 31.2°$ due to the functionalization with Congo red molecules. In the M spectrum, the peaks at 2θ = 30.40°, 32.46°, 34.63°, 37.48°, 40.35°, 42.64°, 53.73°, 55.91°, 56.94°, 62.08°, 63.68°, 64.71°, 68.03°, 73.17°, and 79.01°, which refer to the planes 110, 107, 114, 203, 205, 206, 215, 217, 2011, 2110, 220, 2014, 307, 317, and 3110 indicate that the crystal structure is related to the single

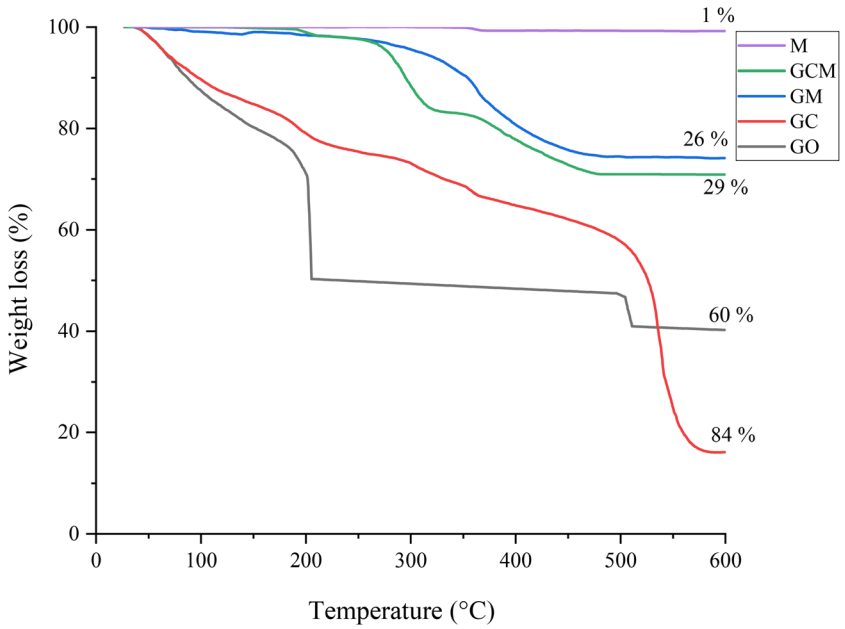

Fig. 9 TGA curves of GO, GC, GM, GCM, and M.

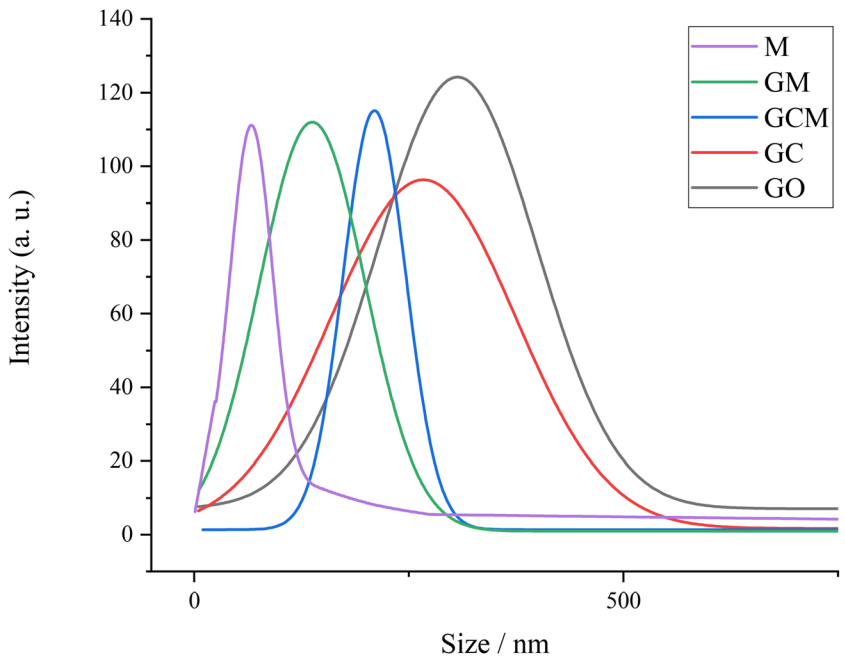

Fig. 10 Particle size distribution of GO, GC, GCM, GM, and M in an aqueous dispersion ($C = 1$ g L^{-1}).

phase of M-type hexagonal barium ferrite $BaFe_{12}O_{19}$, according to the standard card 01-074-1121.[49] In the GM spectra, the 001 plane of the GO peak shifted to higher values as a broad peak around $2\theta = 24.5°$, which is related to the reduction of the graphene surface to rGO during the synthesis of GM.

At the same time, for the other peaks present at $2\theta = 30.29°$, 30.85°, 32.81°, 35.66°, 38.51°, 40.80°, 52.01°, 54.07°, 55.09°, 61.84°, 66.31°, 71.35°, and 77.28°, which are related to the barium ferrite phase, it is noted that the shift in the position and intensity of the peaks from the pure barium ferrite spectra is related to the functionalization of graphene surface with the barium ferrite nanoparticles. Simultaneously, in the GCM spectrum, the peaks at $2\theta = 18.5°$ and 24.45° are attributed to the graphene structure, and the graphene peak of GC at $2\theta = 10.6°$ was shifted to higher values with a broad peak around $2\theta = 24.45°$ for rGO domains, confirming the reduction of the functional groups after GCM formation. The shift from $2\theta = 31.2°$ in GC to 18.5° in GCM can be attributed to the presence of Congo red molecules after functionalization of GC with the barium ferrite nanoparticles. Moreover, the presence of the peaks at around 30.05°, 31.20°, 32.57°, 36.92°, 39.66°, 42.06°, 45.66°, 48.69°, 57.05°, 58.18°, 58.99°, 64.25°, 68.83°, 77.40°, 79.22° is related to the barium ferrite phase, with some shifts in the position and intensity of the peaks owing to the functionalization on the GCM surface.

6.1.3. Energy-dispersive X-ray spectroscopy. Fig. 7 shows the energy-dispersive X-ray (EDX) analysis for GO (A), GC (B), GCM (C), GM (D), and M (E). The EDX spectra display the presence of oxygen in addition to the carbon, owing to the oxygen functional groups on the GO surface. Simultaneously, in the GC spectrum, in addition to the detection of carbon and oxygen, nitrogen and sulfur were also confirmed, proving the functionalization of GO with Congo red molecules. Furthermore, the GCM spectrum exhibits peaks related to carbon, oxygen, nitrogen, iron, barium, and sulfur, which substantiate the successful functionalization of GC with barium ferrite nanoparticles. Additionally, in the GM spectrum, peaks attributed to carbon, oxygen, iron, and barium are detected, confirming the formation of barium ferrite nanoparticles composited with the graphene surface. Moreover, the M spectrum reveals the presence of oxygen, iron, and barium, proving the formation of barium ferrite. The presence of a carbon peak is due to the carbon grid of the sample holder.[50]

6.1.4. UV-visible spectroscopy. Fig. 8 illustrates the UV-visible spectra of water dispersions of GO, Congo red, and GC (Fig. 8A), and M, GM, and GCM (Fig. 8B). Fig. 8A reveals that the GO spectrum shows two absorbance peaks, one at 229 nm and a shoulder peak at around 298 nm, corresponding to the $\pi \rightarrow \pi^*$ and $n \rightarrow \pi^*$ transitions of C–C and C=O bonds, respectively, confirming the oxidation of the graphene surface.[51,52] The UV-Vis spectrum of pure Congo red displays the presence of three peaks at about 230 nm, 320 nm, and 487 nm,[53] while in the GC spectrum, after the conjugation of the GO surface with Congo red, the three peaks were shifted to higher values, at 237 nm, 348 nm, and 531 nm, with smaller intensities with a shift of the GO peak to a lower value of around 197 nm due to the functionalization of GO with Congo red molecules.

Fig. 8B shows the UV-Vis spectrum of M, which contains two absorbance peaks at around 215 nm and 340 nm for barium ferrite nanoparticles. Several factors affect the shift in the absorbance values, such as grain size, band gap, oxygen deficiency, impurities, and surface effects.[54] The peak at 340 nm in pure barium ferrite shifted to higher values in GM (350 nm) and GCM (357 nm) due to the functionalization of barium ferrite

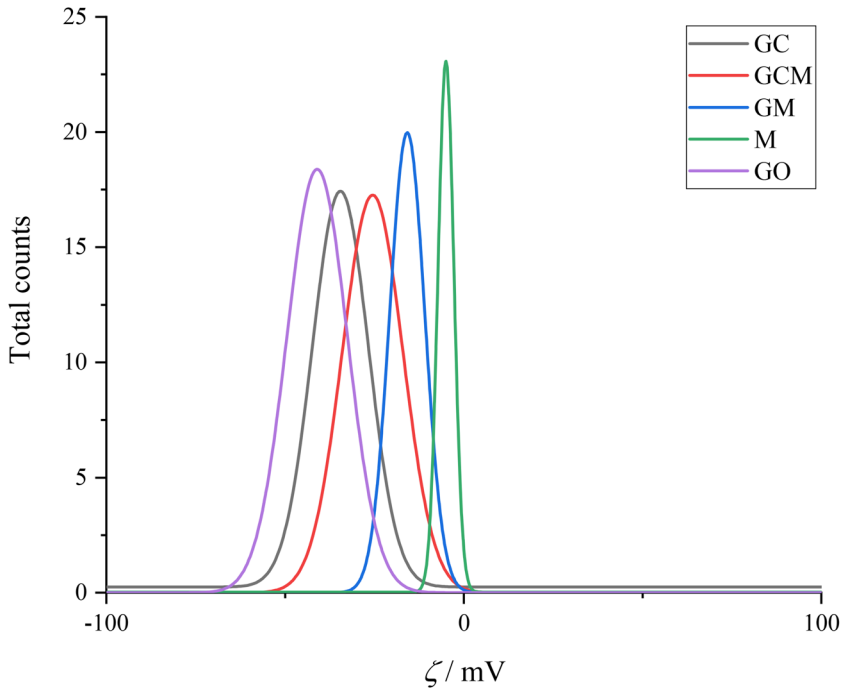

Fig. 11 ζ-Potentials of GO, GC, GCM, GM, and M in an aqueous dispersion ($C = 1$ g L^{-1}).

surface with GO in the GM nanomaterials, and also with GC in the GCM nanoparticles. At the same time, the absorbance peak for M around 215 nm was shifted to slightly higher values in GM, at 218 nm, and also to 231 nm in GCM. Moreover, the absorbance peaks around 297 nm, 415 nm, and 461 nm in GCM are attributed to the Congo red molecules included in the GCM structure, which appear with shifts in the positions of the absorbance peaks due to the functionalization with barium ferrite nanoparticles. The two peaks around 268 nm in both GM and GCM are attributed to the $\pi \rightarrow \pi^*$ transitions assigned to the restoration of the π bonds owing to the reduction of the graphene surface.[52,55–57]

6.1.5. Thermogravimetric analysis. Fig. 9 displays the TGA curves for GO, GC, GM, GCM, and M at room temperature up to 600 °C. Barium ferrite nanoparticles show high thermal stability within this temperature range. At the same time, the GO curve displays gradual degradation with a sudden breakdown at 205 °C due to the release of GO functional groups; further degradation is observed at 507 °C, which is assigned to the decomposition of the basic structure of the carbon skeleton.[58] It is noted that the covalent functionalization of GO with Congo red molecules in the GC nanomaterial leads to higher thermal stability; it began to break down slowly with the degradation of the various functional groups associated with GO and Congo red molecules. Moreover, a rapid degradation is observed at 540 °C, when the carbon skeleton of the GC nanomaterial begins to decompose.

The functionalization of GC with barium ferrite nanoparticles led to an increase in GCM thermal stability. Two mass-loss steps were recorded; the first mass diffraction range is from 270 °C to 320 °C, which is related to the decomposition of the different functional groups of the graphene surface and the Congo red molecules, while the second range of mass loss is located between 360 °C and 475 °C, which is associated with the decomposition of the graphene carbon structure. In comparison, GM reveals greater thermal stability, with a mass loss between 330 °C and 475 °C, which is attributed to the breakdown of the graphene carbon-based skeleton. The weight loss percent is presented in Fig. 9.

6.1.6. Size distribution and ζ-potentials. Fig. 10 indicates the size distribution of the aqueous dispersions of GO, GC, GCM, GM, and M. Analysis of the obtained size distributions reveals that the nanoparticles of GO, GC, GCM, GM, and M have sizes of around 305 nm, 270 nm, 210 nm, 138 nm, and 66 nm, respectively. At the same time, the ζ-potentials obtained were −41 mV, −34 mV, −25 mV, −15 mV, and −5 mV for GO, GC, GCM, GM, and M, respectively (Fig. 11). These values prove that GO, GC, and GCM exhibit higher dispersion stability, which is associated with the various functional groups on their surfaces, while GM and M showed less dispersion stability.

6.1.7. Vibrating sample magnetometry. Fig. 12 demonstrates the magnetic hysteresis loops of (A) M, GCM, and GM, and (B) GO and GC *via* the VSM technique at room temperature. Fig. 12A shows that barium ferrite has higher saturation magnetization (M_s) and coercivity (H_c) than GCM and GM. M_s values are 59 emu g^{-1}, 35 emu g^{-1}, and 25 emu g^{-1} for M, GCM, and GM, respectively. It is evident that M has M_s value that is consistent with prior reports,[59] and the reduction in M_s value for GCM and GM is attributed to the presence of spin disordered surface layers[60] due to the existence of defects as multiple pores found on the graphene surface as observed from the SEM pictures with the magnetic nanoparticles spread inside and outside the pores, in addition to the decreased size of magnetic nanoparticles in GM and GCM as a result of the synthesis process, this can disrupt the magnetic spin orientation. The incorporation of graphene domains with magnetic nanoparticles can lead to a random orientation of spins; thus, a decrease in the saturation magnetization was observed for the graphene ferrite composites.[61]

H_c for barium ferrite is around 2183 Oe, whereas for GCM and GM, it was significantly reduced to 212 Oe and 147 Oe, respectively. It is observed that M, GM, and GCM have ferrimagnetic properties; while M shows hard magnetic behavior, GCM and GM exhibit soft magnetic character with larger M_s for GCM than for GM. This can be ascribed to the functionalization of the graphene surface with Congo red molecules with

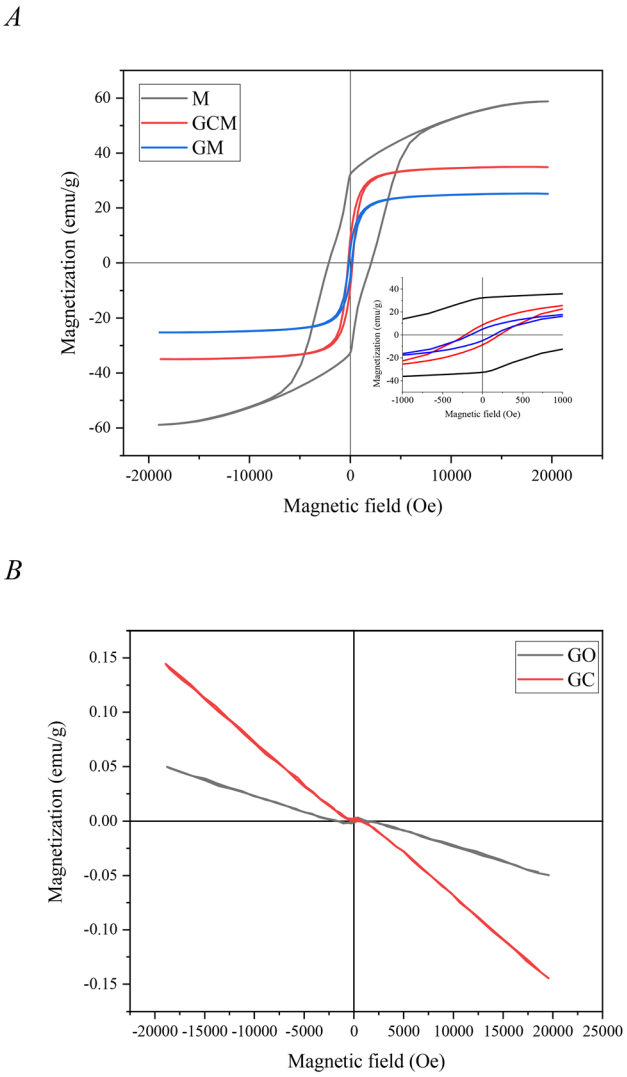

Fig. 12 Magnetic hysteresis loops of (A) M, GCM, and GM, and (B) GO and GC.

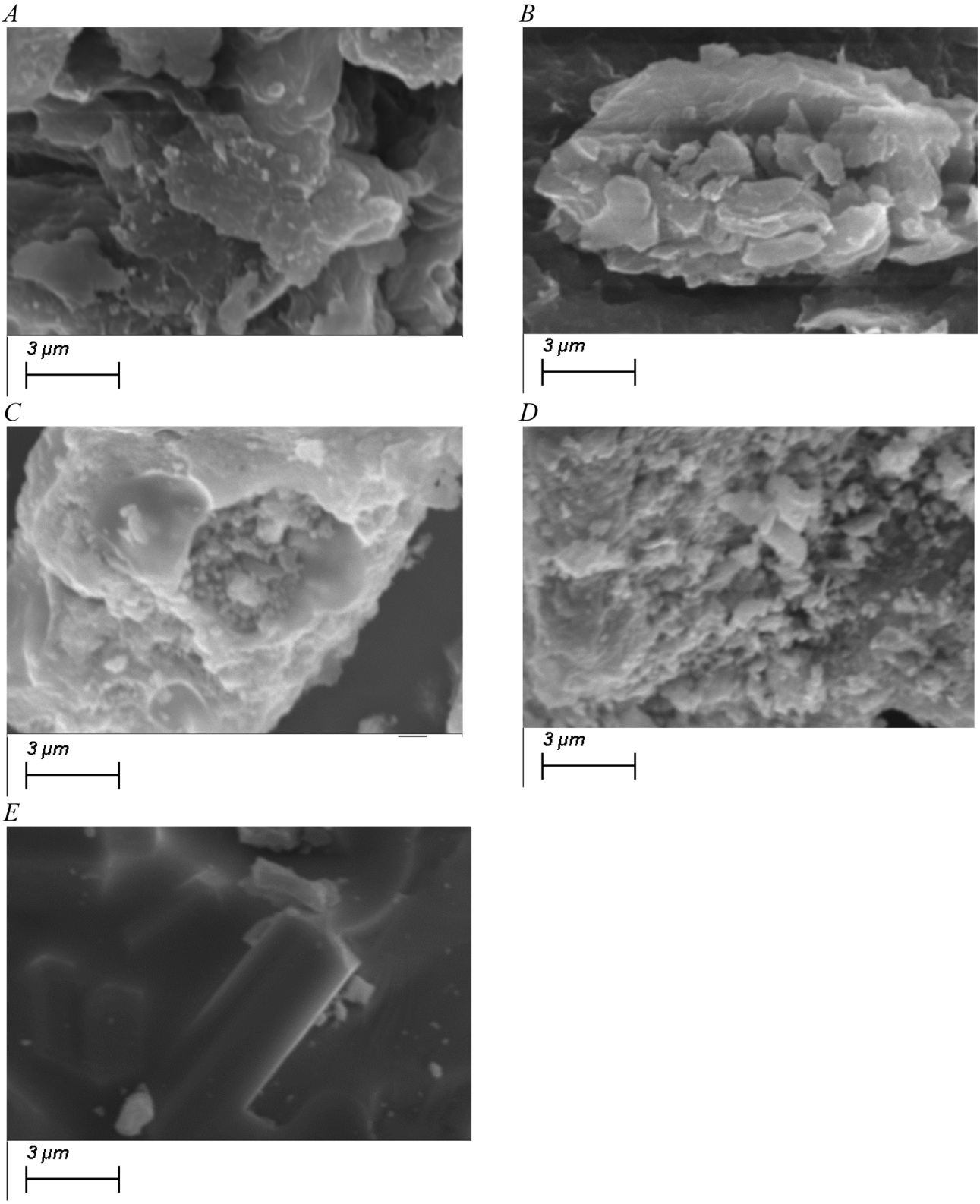

Fig. 13 SEM study for GO (A), GC (B), GCM (C), GM (D), and M (E).

increased interlayer distances and less magnetic spin disorder.[60] The reduction in the M_s value after incorporation of graphene with barium ferrite was previously reported.[62] On the other hand, Fig. 12B illustrates that GO and GC bear predominantly diamagnetic characteristics; the diamagnetic response of graphene oxide was introduced in different studies.[63–65] A diamagnetic material is weakly repelled by an external magnetic field, an effect that arises from slight changes

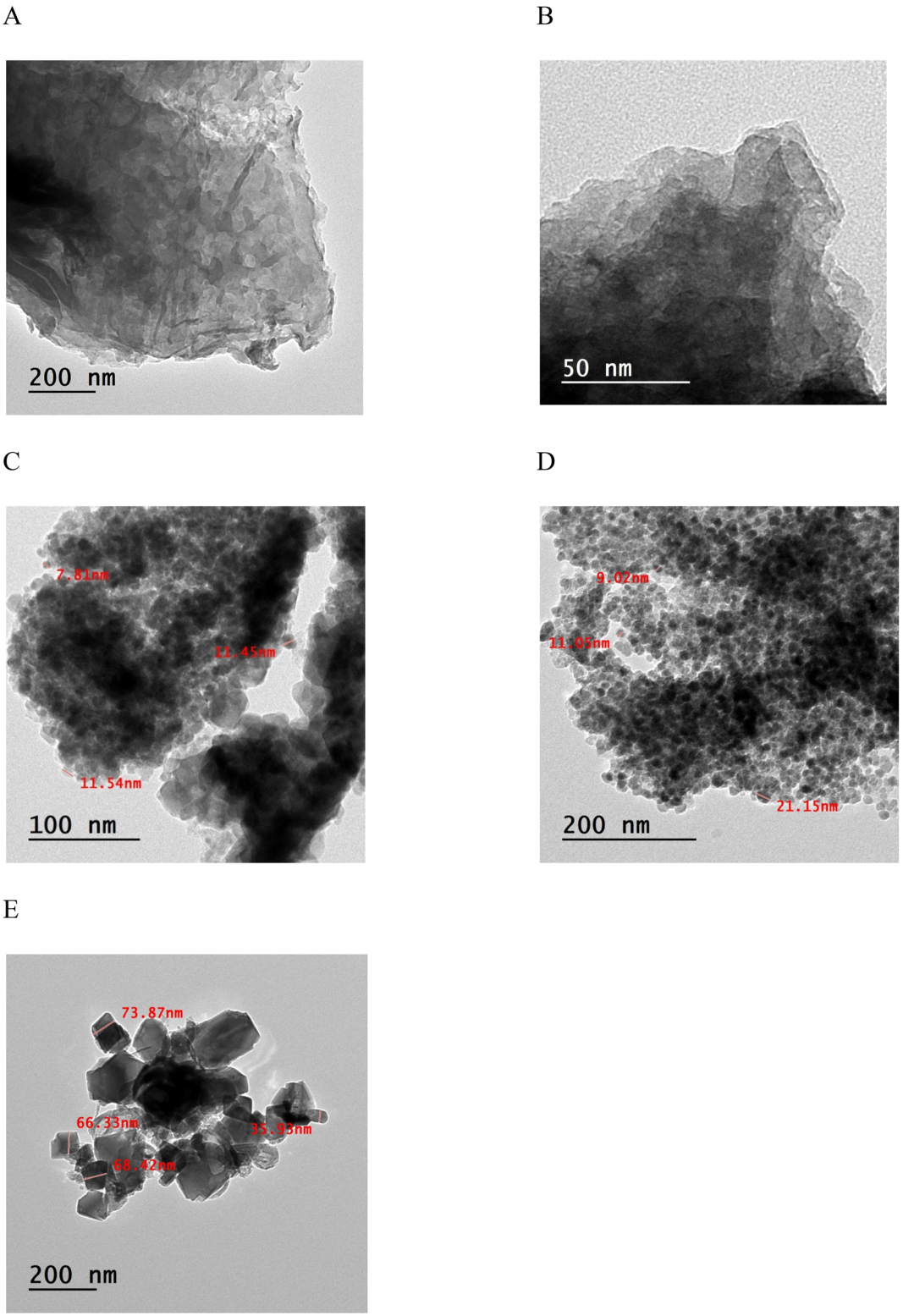

Fig. 14 HRTEM images for GO (A), GC (B), GCM (C), GM (D), and M (E).

in the orbital dynamics of electrons, leading to a weak magnetic response.[66]

It is noted that the integration of barium ferrite with rGO or GC can soften the hard ferrimagnetic material; this feature can qualify both GM and GCM for future applications in the field of nanorobots owing to the ease of magnetization and demagnetization, which facilitates precise external control and propulsion, in addition to decreased aggregation and lower toxicity. This soft ferrimagnetic nature can also avoid uncontrolled attractions between particles inside blood vessels or tissues,

which is promising for biomedical robotic applications, especially for minimally invasive medicine, targeted drug delivery, imaging, hyperthermia, and theranostics.[67–71] An external magnetic field can also be used to remove the robotic magnetic material from the body after task completion.[72]

6.1.8. Scanning electron microscopy. Fig. 13 illustrates the morphology of GO (A), GC (B), GCM (C), GM (D), and M (E) using SEM analysis. From Fig. 13, it is clear that the GO flakes appear as separated sheets with sharp edges, while after functionalization with Congo red molecules, the graphene flakes in GC were transformed into softer sheets with a shiny surface; this can be attributed to the distinguished optical and fluorescence properties of Congo red molecules attached to the graphene surface.[73] The morphology study of the GCM and GM surfaces demonstrates the appearance of pores or voids of different sizes that load tiny particles of the barium ferrite nanomaterial inside

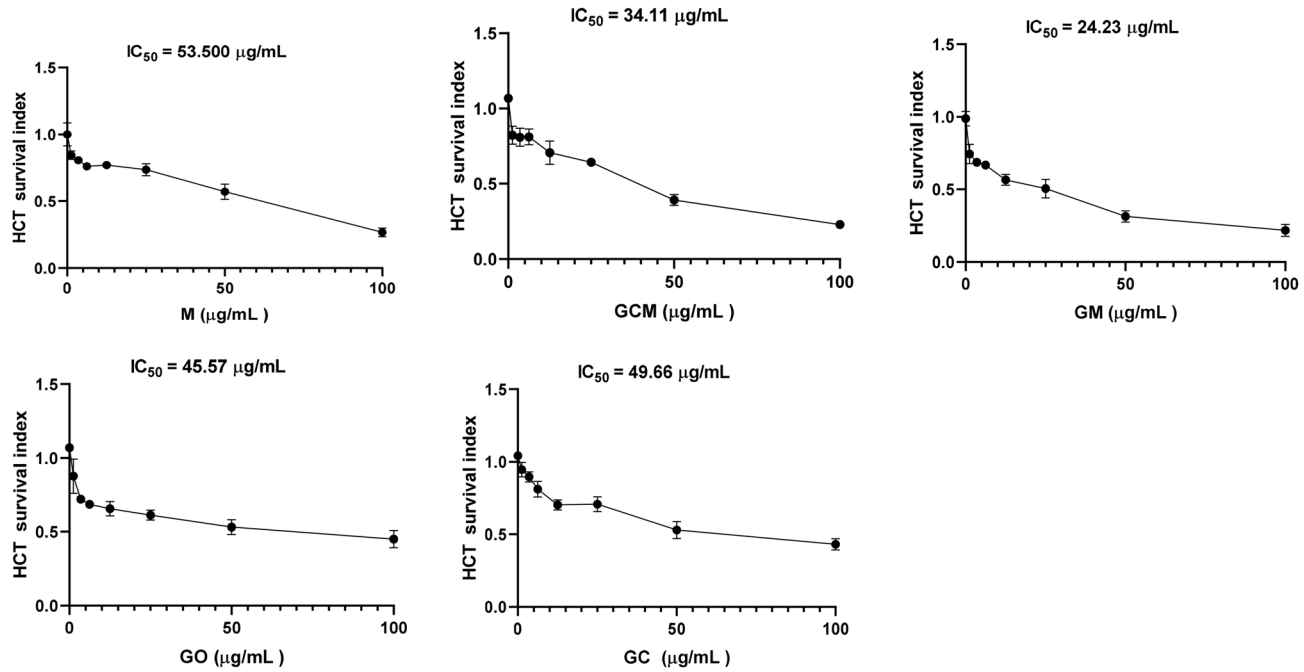

Fig. 15 IC_{50} of the tested compounds on the HCT 116 cell line.

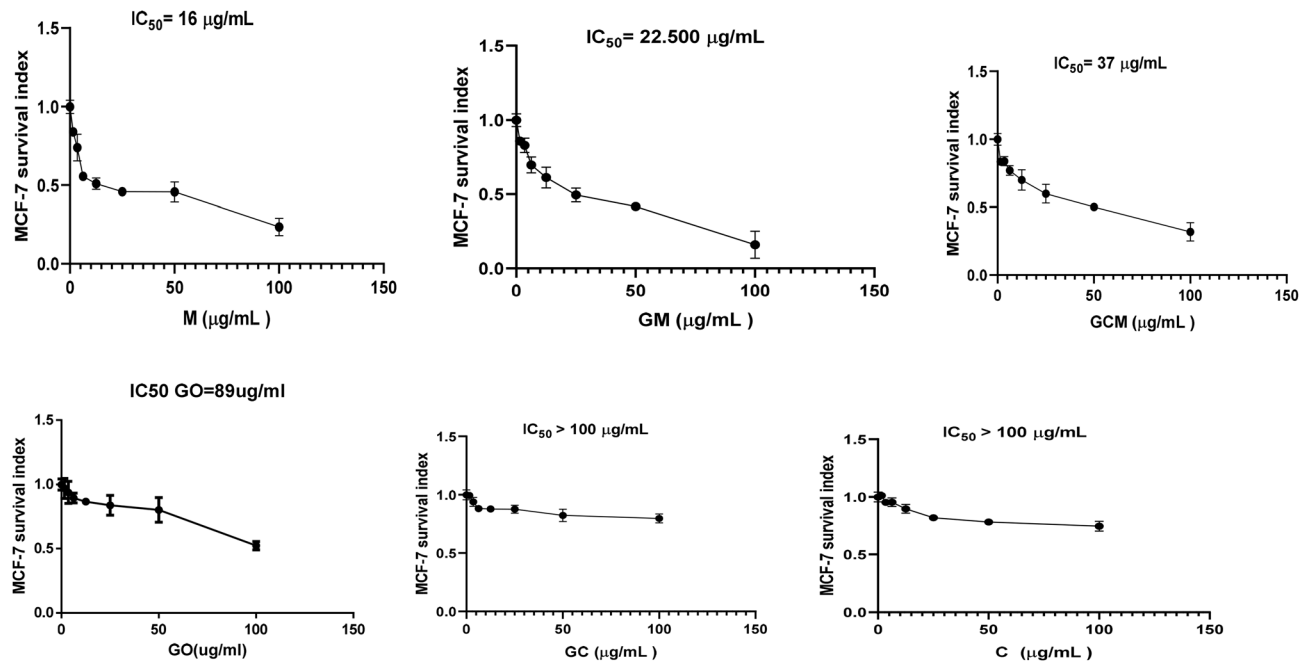

Fig. 16 IC_{50} of tested compounds on the MCF-7 cell line.

Table 1 IC_{50} of tested compounds on the Vero, HCT 116, and MCF-7 cell lines

Compound	IC_{50} (μg mL^{-1}) on Vero cells	IC_{50} (μg mL^{-1}) on HCT116	IC_{50} (μg mL^{-1}) on MCF-7
GO	>100	45.6	89
M	>100	53	16
GM	>100	24	22.5
GC	>100	49.6	>100
GCM	>100	34	37
C	>100	>100	>100

and outside the cavities. Furthermore, the SEM analysis for barium ferrite nanoparticles demonstrates hexagonal shapes with higher particle size of M in comparison with the ferrite nanoparticles distributed on GM and GCM because of being incorporated in different synthesis conditions in the presence of graphene sheets.

6.1.9. High-resolution transmission electron microscopy. Fig. 14 indicates the results of the morphology study using HRTEM for GO (A), GC (B), GCM (C), GM (D), and M (E). The GO image presented in Fig. 14A shows that GO is made up of several flakes. At the same time, Fig. 14B shows more transparent layers for GC related to increased interlayer distances, with the appearance of some agglomerations due to the functionalization of GO with Congo red molecules. Meanwhile, the GCM image, displayed in Fig. 14C, shows agglomerations of dark spots of around 11 nm homogeneously distributed all over the GCM surface, confirming the successful functionalization of GC with barium ferrite nanoparticles. Fig. 14D demonstrates that the GM surface has dark spots uniformly distributed on the graphene surface with a diameter of 21 nm, proving the functionalization of graphene with barium ferrite nanoparticles; furthermore, GCM seems to have a softer aspect when compared with GM. Finally, Fig. 14E shows the morphology of the barium ferrite nanoparticles, with hexagonal shapes and particle sizes of around 73 nm. The decreased particle size of barium ferrite in GM and GCM in comparison with M is attributed to the different synthesis conditions of each. Pure barium ferrite was prepared using the sol–gel auto-combustion method and calcined at 900 °C. GCM was prepared after strong mechanical forces were applied to the GC–barium ferrite mixture, reducing its particle size. For GM, the incorporated barium ferrite nanoparticles were synthesized through a one-pot *in situ* synthesis in which GO was included with the sol–gel auto-combustion process. The entrapment of the ferrite particles on the graphene surface can protect the ferrite nanoparticles from agglomerations caused by elevating the temperature during calcination.

Table 2 Concentration of cellular DNA of HCT116 treated with the selected materials

No	Sample	Conc. ng mL^{-1}
1	Ladder 100 bp	
2	Cell control	137.2
3	M	126.9
4	GM	108
5	GCM	59.4
6	GO	130
7	GC	98.8

Table 3 Concentration of cellular DNA of MCF-7 treated with the selected materials

No	Sample	Conc. ng mL^{-1}
1	Ladder 100 bp	
2	Cell control	279.4
3	C	192.8
4	GO	93.3
5	GM	149.2
6	GCM	133
7	GC	52.8
8	M	168

6.2 Bioactivity study

6.2.1. MTT assay. Fig. 15 and 16 and Table 1 present the IC_{50} values of the GO, GC, M, GM, GCM, and pure Congo red molecules (C) on the human cancer cells (HCT 116 and MCF-7) and Vero normal cells. Analysis of the results revealed that GM

Table 4 Quantitation of the expression of some apoptotic genes after 24 h of cell exposure on a transcriptional level for HCT116[a]

Treatment	Caspase 3 RQ 2	BCL2 RQ $2^{-\Delta\Delta CT-\Delta\Delta CT}$	Bax RQ 2	P53 RQ $2^{-\Delta\Delta CT-\Delta\Delta CT}$
Cell control	1	1	1	1
GO	0.62	23.5	0.44	0.34
M	1.64	2.02	17.26	8.16
GM	2.56	0.52	5.5	7.51
GC	2.37	0.9	2.46	200.85
GCM	8.45	0.80	245.5	8.11

[a] RQ < 1 is considered downregulation, whereas RQ > 1 is considered upregulation.

Table 5 Quantitation of the expression of some apoptotic genes after 24 h of cell exposure (caspase 3, Bax and anti-apoptotic BCL2, and P53) on a transcriptional level for MCF-7[a]

Treatment	Caspase 3 RQ 2	BCL2 RQ $2^{-\Delta\Delta CT-\Delta\Delta CT}$	Bax RQ 2	P53 RQ $2^{-\Delta\Delta CT-\Delta\Delta CT}$
Cell control	1	1	1	1
C	6.5	0.29	1.55	1.21
GO	139.1	0.059	12.55	1.63
GM	28.64	0.00025	91.13	1.05
GCM	2.44	0.76	1.14	3.11
GC	25.28	0.053	3.2	1.74
M	3.45	0.075	2.78	1.23

[a] RQ < 1 is considered downregulation, whereas RQ > 1 is considered upregulation.

and GCM exhibited the highest potency, with IC_{50} values of 24 and 34 μg mL^{-1}, respectively, for HCT, 116 and 22.5 and 37 μg mL^{-1}, respectively, for MCF-7 cells, indicating their antiproliferative activity against the tested cancer cells. Regarding M, it demonstrated high antiproliferative activity against MCF-7 (IC_{50} = 16 μg mL^{-1}) but a weaker effect on HCT116 (IC_{50} = 53 μg mL^{-1}). GO and GC demonstrated moderate cytotoxicity (IC_{50} = 45.6 and 49.6 μg mL^{-1}, respectively, for HCT 116, and 89 and >100 μg mL^{-1}, respectively, for MCF-7). In contrast, Congo red (C) was safe for all the tested cancer cells (IC_{50} > 100 μg mL^{-1}). Regarding the results on Vero cells as a model of normal cells, all tested compounds were safe (IC_{50} > 100 μg mL^{-1}). These observations demonstrate how physicochemical properties and the design of the nanomaterials affect the cellular interactions, which, in turn, affect uptake *via* the cell membrane, resulting in varying degrees of cell viability.[74]

In addition, results might indicate a synergistic effect of combining the graphene surface with the magnetic nanomaterials, which leads to enhanced anti-proliferative activity because it may target multiple cellular pathways, maximizing their effect on cancer cells without harmful impact on normal cells. Furthermore, Congo red functionalization (GCM) showed comparable efficacy to GM, suggesting its role as a targeting ligand that leverages both the surface morphology and the soft magnetic properties of the nanomaterial system to enhance therapeutic delivery without compromising safety.[17] It is observed that whereas pure Congo red did not show cytotoxicity for any of the cancer cells, the moderate antiproliferative activity of graphene derivatives (GO and GC) increased after combination with barium ferrite in both GM and GCM. This observation can confirm the synergistic effect of the graphene surface and the barium ferrite nanoparticles as cytotoxic agents for cancer cells. The Congo red conjugation with the graphene surface can enhance the specificity for cancer cells through binding to the β sheets of amyloid-like aggregates in cancer cells, which are not found in normal cells. This can enhance the ability of the hybrid nanomaterial to detect and target cancer cells and inhibit mutant p53 aggregation, thereby restoring its transcriptional activity and suppressing the growth of the tumor while decreasing the cytotoxicity toward normal cells.[26–29] The targeting ability of Congo red molecules, alongside the high surface area of graphene sheets and the Fenton reaction activity enhanced by the ferrite nanoparticles,[31] increases the ability of GCM nanomaterials to act as antiproliferating agents to suppress cancer growth. Moreover, the acquired soft ferrimagnetic behavior due to reduced coercivity can facilitate GCM applications in magnetic hyperthermia for cancer treatment.[75,76]

The unique cytotoxicity exhibited by magnetic nanoparticles is due to the specific redox nature of tumors. All malignant cells maintain a high basal level of hydrogen peroxide (H_2O_2) in comparison to normal cells.[77,78] Iron oxide nanoparticles, in particular iron-based ferrites, can take advantage of this disparity using Fenton reactions. In these reactions, the Fe^{2+}/Fe^{3+} ions on the surface of the NPs also react with H_2O_2 to produce hydroxyl radicals (·OH), which are the most toxic ROS.[79,80] As a result of the high endogenous H_2O_2 levels in the tumor environment, this catalytic process is notably enhanced in cancer cells. The resulting increase in ·OH generation results in intense oxidative stress, inducing cell apoptosis.[81–83]

Morphological examination confirmed such harmful effects on the tested cell lines. Based on IC_{50} results, further analysis on a molecular level was performed for all the tested materials on both cancer cell lines.

6.2.2. DNA fragmentation. The nature of cell death on a molecular level was investigated using a DNA fragmentation assay. Regarding HCT116 (colon cancer cell line), GCM (graphene–Congo red–barium ferrite) showed the most pronounced DNA damage, reducing DNA concentration to 59.4 ng mL^{-1}

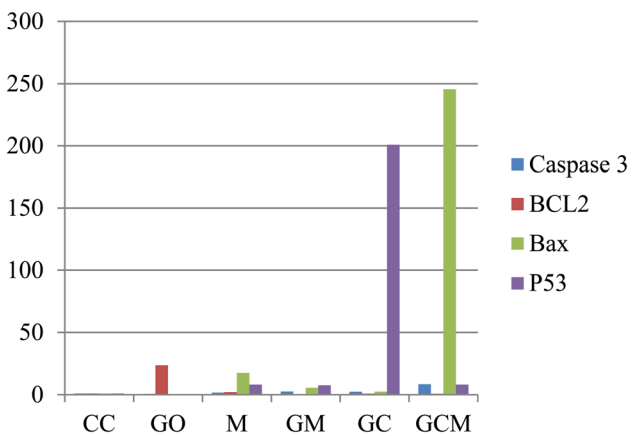

Fig. 17 Quantitation of the expression of some apoptotic genes after 24 h of cell exposure on a transcriptional level.

(*versus* 137.2 ng mL^{-1} for untreated cells), but GC and GM induced lesser effects (98.8 and 108 ng mL^{-1}, respectively) as shown in Table 2. For MCF-7 (breast cancer cell line), GC exhibited the highest activity, reducing DNA content to 52.8 ng mL^{-1} (*versus* 279.4 ng mL^{-1} for untreated cells) as shown in Table 3. In contrast to the effect on the HCT116 cell line, GCM showed a moderate effect on the MCF-7 cell line, where the DNA content was 133 ng mL^{-1}. These results align with the cytotoxicity trends observed in the MTT assay, confirming that Congo red-functionalized nanomaterials (GC/GCM) preferentially target cancer cell DNA.

6.2.3. Quantitative apoptotic gene expression, detected using the RT-PCR assay on tested cancer cells. The apoptotic effect was investigated using qRT-PCR analysis to examine the mechanism of the anti-proliferative activity of the nanomaterials against HCT116 and MCF-7 cell lines. The results showed that the nanomaterials induced apoptosis *via* the intrinsic caspase-dependent pathway with the following details:

Pro-apoptotic markers, including mRNA expressions of caspase 3, BAX, and P53 genes, were up-regulated (RQ > 1) in both cell lines (Tables 4 and 5, Fig. 17 and 18). For HCT116, GCM triggered the highest caspase 3 and Bax expressions (RQ = 8.45 and 245.5, respectively), whereas on MCF-7, GO induced extreme caspase 3 (RQ = 139.1), while GM induced the expression of Bax (RQ = 91.13). Regarding the anti-apoptotic marker, BCL2 was downregulated (RQ < 1) across all treatments, notably for the MCF-7 cell line, and GM showed the strongest suppression of BCL2 expression (RQ = 0.00025). All the results matched; thus, GM/GCM drive mitochondrial dysfunction by upregulating Bax and downregulating BCL2 gene expression. Further insightful analysis on other apoptotic gene profiles and cell cycle analysis is needed to identify the exact targets that can effectively control the proliferation of human colon cancer cell lines and human breast cancer cells.

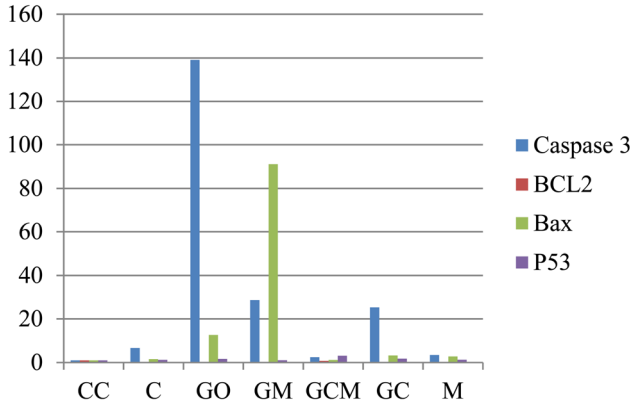

Fig. 18 Quantitation of the expression of some apoptotic genes after 24 h of cell exposure (caspase, Bax and anti-apoptotic BCL2, and P53) on a transcriptional level for MCF-7.

6.3 *In silico* studies

6.3.1. Docking target. Among the predicted proteins, P08575, corresponding to Receptor-type Tyrosine-Protein Phosphatase C (PTPRC/CD45), exhibited a probability value of 1.0, indicating maximal confidence in the predicted interaction. This strong prediction suggests that the compound aligns closely with the QSAR models associated with CD45, making P08575 a compelling biological target. CD45 is a leukocyte-specific receptor-type tyrosine phosphatase that regulates Src-family kinases, which serve as key upstream controllers of

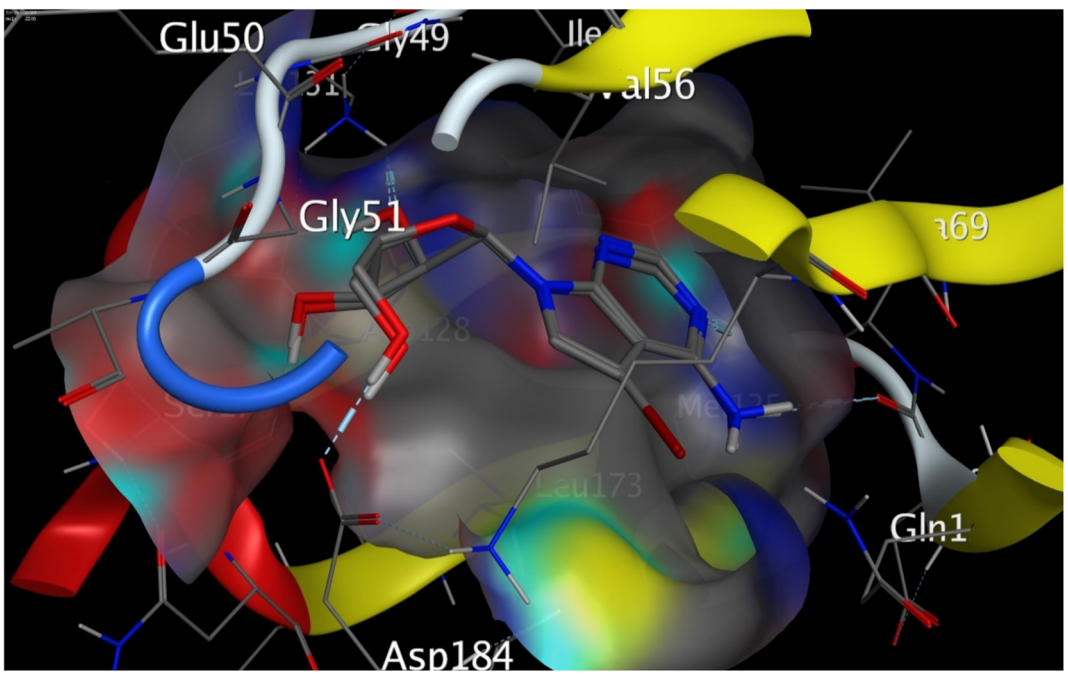

Fig. 19 3D-visualization showing the alignment of the docked and the co-crystallized ligand in the pocket of the active site of the receptor.

major oncogenic pathways, including PI3K/AKT, MAPK/ERK, and JAK/STAT.[84–86] Dysregulation of these pathways is well recognized in cancer biology for promoting survival, proliferation, resistance to apoptosis, and malignant transformation.[87–90] Altered CD45 activity, as noted in several hematological malignancies, can enhance proliferative signaling and suppress apoptotic pathways. Conversely, modulation of CD45 function can restore apoptotic responses by activating p53, increasing caspase-3 activity, and shifting the BAX/Bcl-2 ratio towards a pro-apoptotic state, collectively contributing to antiproliferative effects. Thus, a compound predicted to strongly interact with CD45 may influence these apoptotic and antiproliferative pathways, reinforcing the mechanistic relevance of selecting P08575 as a docking target.

To translate the predicted target identity into a structural model for docking, the Protein Data Bank entry 2ZOQ was chosen.[91] The 2ZOQ crystal structure corresponds directly to the catalytic D1 domain of CD45;[85,92] the same protein was identified by TargetNet under UniProt P08575.[93] This structure provides the experimentally resolved three-dimensional conformation of the active phosphatase domain responsible for substrate dephosphorylation and modulation of downstream oncogenic signaling pathways. Because 2ZOQ represents the functional region of CD45 and offers a high-quality, X-ray-derived protein structure, it is an appropriate and scientifically justified model for docking studies.[94] Its direct correspondence to the predicted target ensures consistency between the computational target prediction and the structural docking analysis, enabling accurate investigation of the potential binding interactions of the sodium-free Congo red molecule with CD45.

5-Iodotubercidin is a known small-molecule inhibitor of several protein kinases, including adenosine kinase (ADK) and certain tyrosine kinases, and has been reported to exhibit cytotoxic and pro-apoptotic effects in various cancer cell models.[95]

5-Iodotubercidin has been shown to interact with ATP-binding sites of kinases and phosphatases, which share structural similarity with the catalytic domain of CD45. This makes it a relevant reference compound for *in silico* docking studies with 2ZOQ, a crystal structure of the CD45 phosphatase domain.

6.3.2. Docking validation. Validation of the docking protocol was first performed by re-docking 5-iodotubercidin, the native anticancer inhibitor co-crystallized in the CD45 structure (PDB ID: 2ZOQ), into the protein's active site. The re-docked ligand adopted a binding orientation highly comparable to the experimentally observed conformation, confirming the reliability of the docking procedure. As illustrated in Fig. 19, the docked pose aligned closely with the co-crystallized ligand within the active-site pocket, effectively reproducing the established pharmacophore interactions. The calculated root-mean-square deviation (RMSD) between the crystallographic ligand and the re-docked pose was 0.20 Å, indicating excellent structural overlap. RMSD values below 2 Å are generally considered indicative of a robust and reliable docking protocol;[96] therefore, this exceptionally low RMSD confirms that the applied docking

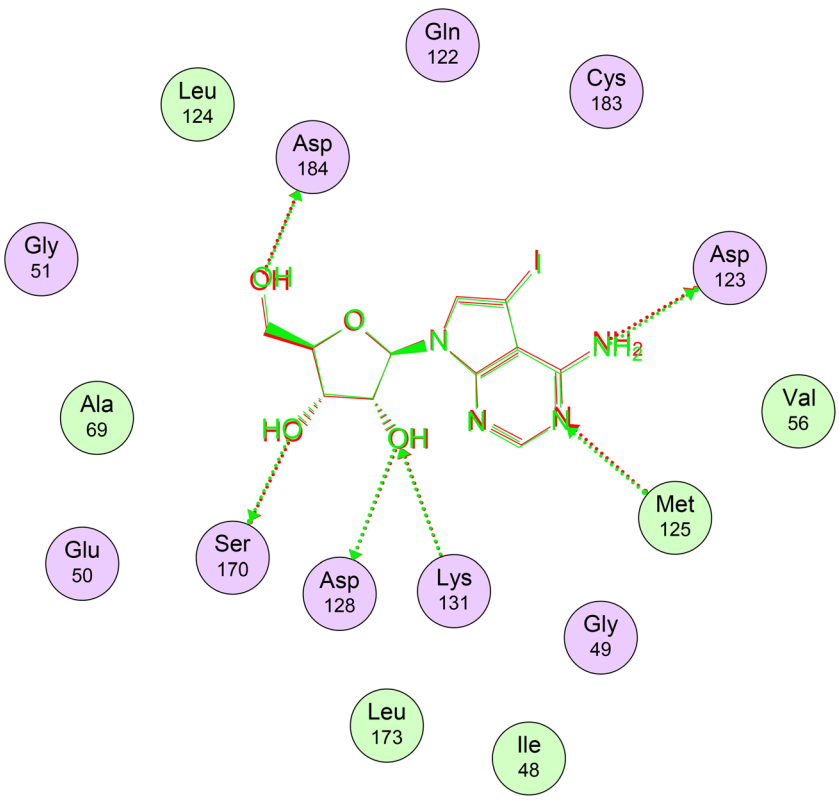

Fig. 20 2D depiction showing the relative binding of the co-crystallized structure and the docked structure with the active site residues of the 2ZOQ protein.

settings are appropriate for predicting ligand binding in the CD45 active site. The docking score of the re-docked compound was −15.00 kcal mol^{-1}, further suggesting favorable binding affinity and accurate pose prediction.

The interaction analysis between the ligand and the CD45 active site (2ZOQ) indicates a strong correspondence between the co-crystallized and docked ligand poses. All key hydrogen-bonding interactions observed in the co-crystallized ligand were successfully reproduced in the docked ligand, with only minor variations in bond distances, as illustrated in the 2D depiction (Fig. 20).

Quantitative comparison of the binding interactions is presented in Table 6, which summarizes the hydrogen-bond distances and corresponding interaction energies for both the co-crystallized and docked ligands. The slight variations in hydrogen-bond lengths and energies reflect minor adjustments in binding geometry during computational optimization, yet the core interactions remained intact. Collectively, these findings confirm that the chosen docking protocol reliably reproduces experimentally validated binding modes, supporting its use for subsequent docking simulations with the test ligands involving Congo red, and the representative small graphitic sectors of GC and rGO included in GCM and GM platforms, respectively (after excluding barium ferrite nanoparticles).

For instance, the H–donor interaction between O5′ and OD2 of ASP 184 slightly increased from 2.41 Å to 2.60 Å upon docking, while interactions with ASP 123, ASP 128, and SER 170 showed minimal distance changes (<0.25 Å). The H–acceptor contacts with MET 125 and LYS 131 were maintained with negligible variation. Interaction energies of the docked ligand were generally comparable to or slightly more favorable than those of the co-crystallized ligand, notably the O2′–OD2 (ASP 128) and O3′–O (SER 170) interactions, which became more stabilizing. Overall, these findings confirm that the docking protocol accurately reproduced the native binding mode, maintaining key hydrogen bonds within the active site and supporting the reliability of subsequent docking predictions (Table 6).

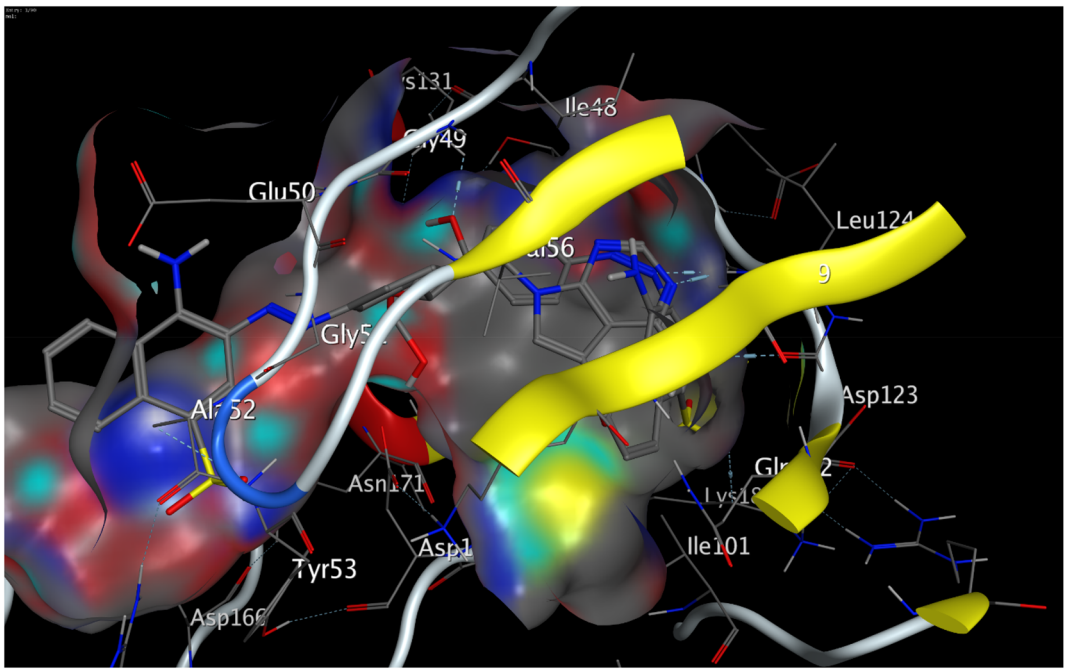

Fig. 21 3D-visualization showing the stereo fitting of Congo red in the pocket of the active site of 2ZOQ.

Table 6 Quantitative interaction of both the co-crystallized ligand and its re-docked structure with amino acid residues of the 2ZOQ active site

			Co-crystallized ligand		Docked ligand	
Ligand atom	Receptor residue	Interaction type	Distance (Å)	Distance (Å)	E (kcal mol^{-1}) report 1	E (kcal mol^{-1}) report 2
O5′ 1	OD2 ASP 184 (A)	H–donor	2.41	2.60	11.2	−2.6
N6 22	O ASP 123 (A)	H–donor	2.75	2.81	−1.8	−1.0
O2′ 27	OD2 ASP 128 (A)	H–donor	2.52	2.70	−2.7	−4.6
O3′ 31	O SER 170 (A)	H–donor	2.51	2.75	0.3	−2.9
N1 17	N MET 125 (A)	H–acceptor	3.09	3.09	−3.8	−3.8
O2′ 27	NZ LYS 131 (A)	H–acceptor	2.77	2.89	−1.5	−1.1

6.3.3. Molecular docking of Congo red. Following validation of the docking protocol, Congo red was docked into the active site of the target protein using the established computational pipeline. The resulting docked pose demonstrated a strong and well-defined fit within the active-site cavity, indicating favorable steric complementarity and appropriate ligand orientation. As illustrated in Fig. 21, the ligand occupies the same binding pocket as the reference inhibitor, maintaining a stable position.

The alignment of Congo red with the co-crystallized inhibitor further supports the reliability of the docking model. Structural superposition (Fig. 22) demonstrated that Congo red closely overlaps with the reference ligand within the active-site pocket, indicating that it adopts a biologically relevant binding

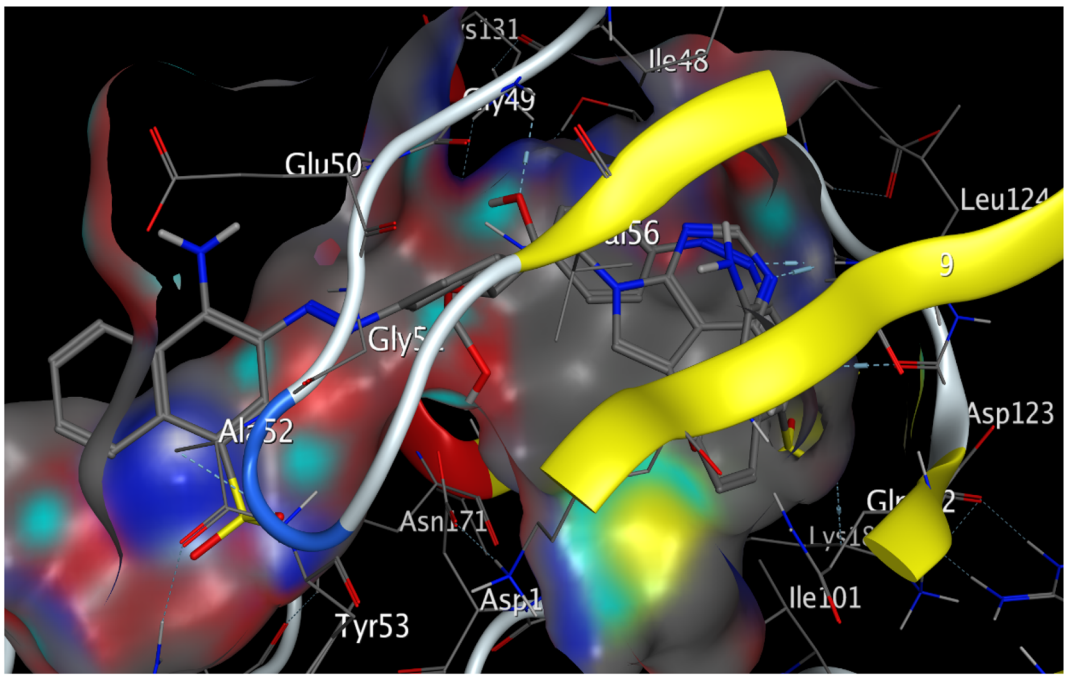

Fig. 22 3D-visualization showing the alignment of Congo red and the co-crystallized inhibitor in the pocket of the active site of 2ZOQ.

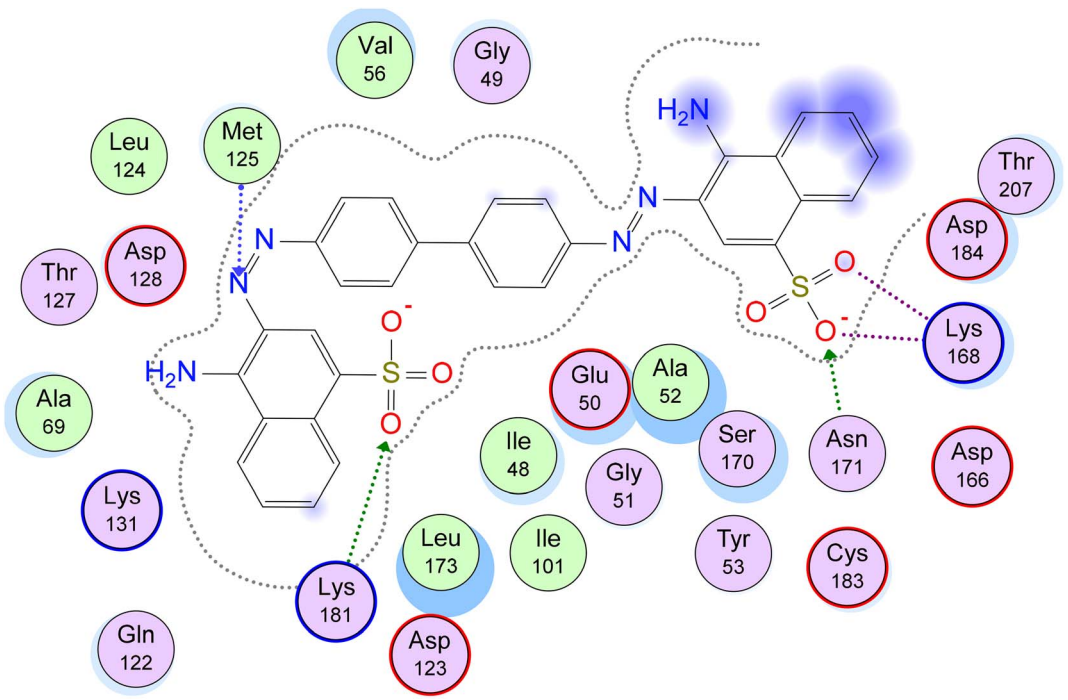

Fig. 23 2D depiction showing the binding modes of the Congo red structure and the target protein residues.

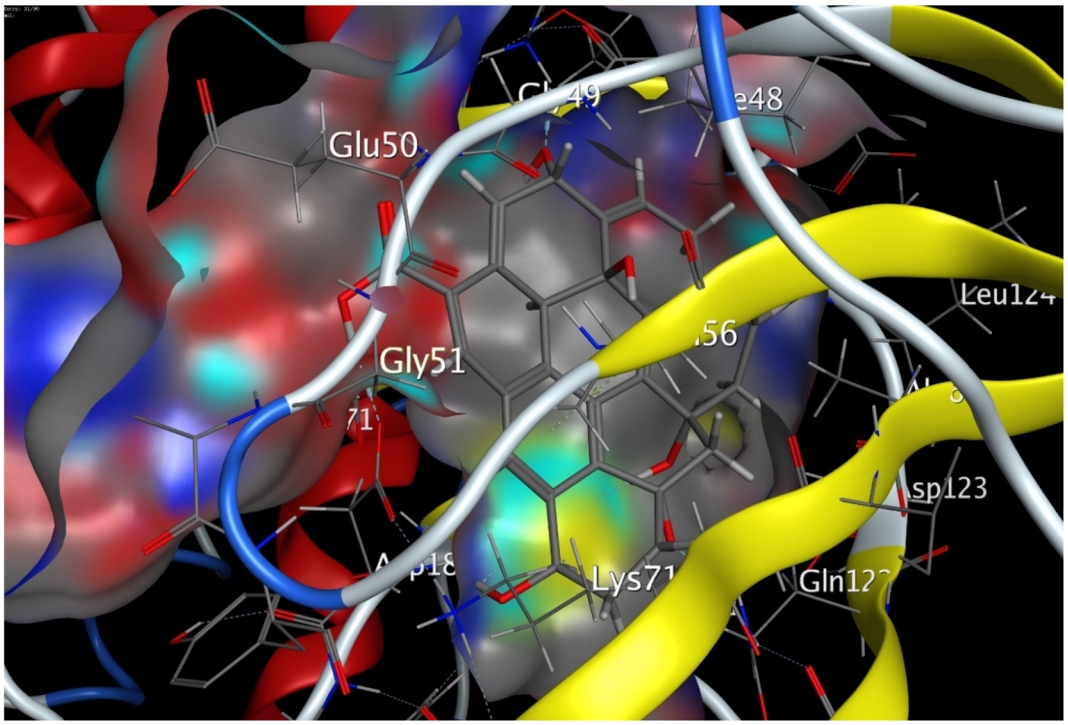

Fig. 24 3D-visualization showing the stereo fitting of rGO in the pocket of the active site of the receptor.

orientation. The calculated RMSD of 1.98 Å between the experimental ligand and the predicted Congo red pose falls within the accepted threshold for reliable docking validation, confirming the consistency of the docking protocol. Moreover, Congo red achieved a docking score of −22.10 kcal mol^{-1}, reflecting a strong predicted binding affinity and reinforcing its potential as an effective binder to the target protein.

The ligand interaction analysis revealed several key stabilizing contacts between the docked compound and residues within the active site of the target protein (Fig. 23). The ligand

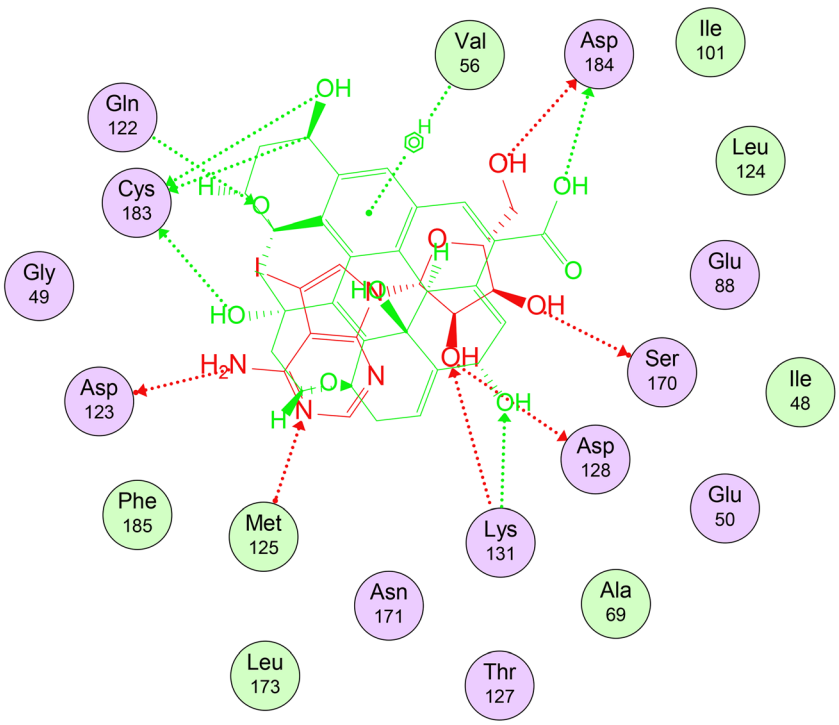

Fig. 25 2D-visualization showing the alignment of GO and the co-crystallized inhibitor in the pocket of the active site of 2ZOQ.

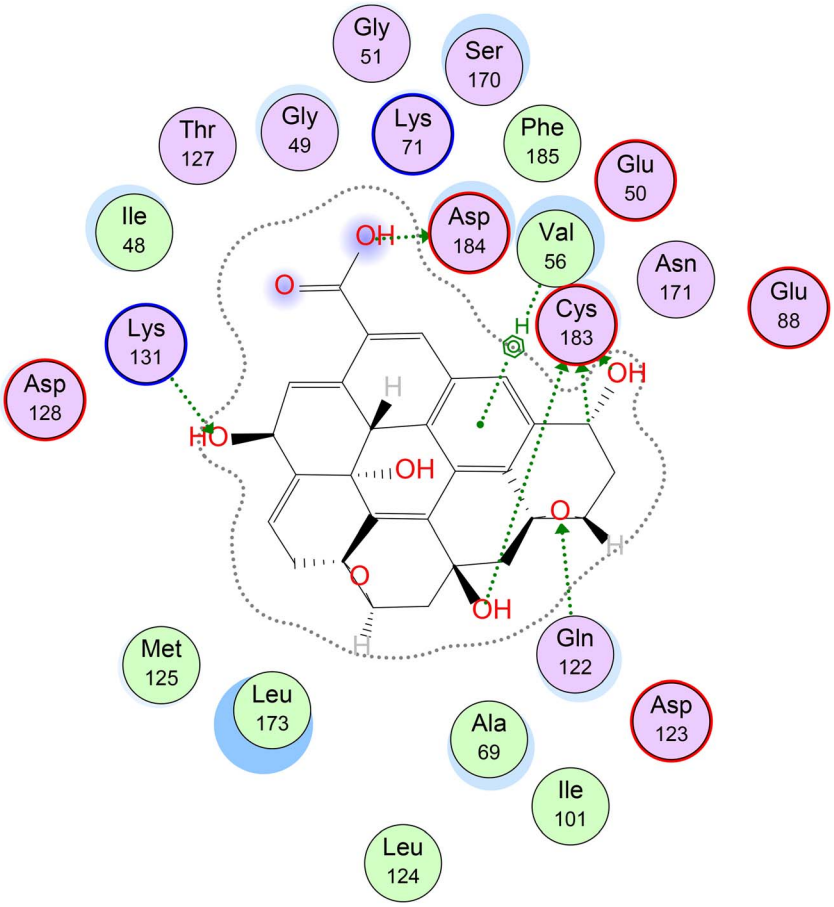

Fig. 26 2D depiction showing the binding modes of the rGO structure with protein residues of 2ZOQ.

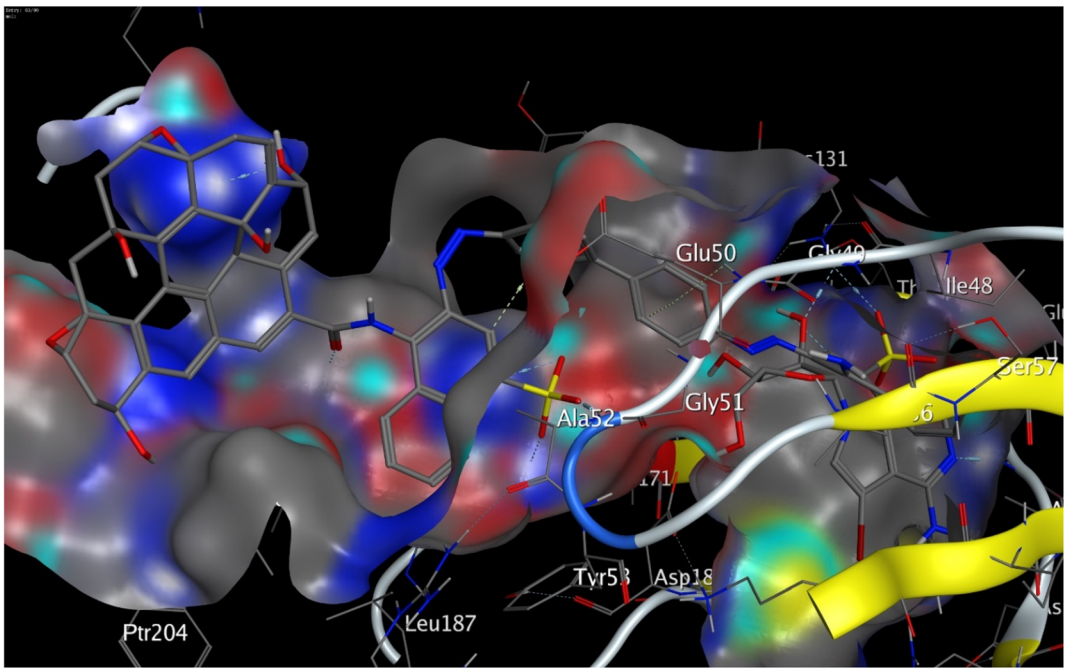

Fig. 27 3D-visualization showing the stereo fitting of GC in the pocket of the active site of the receptor.

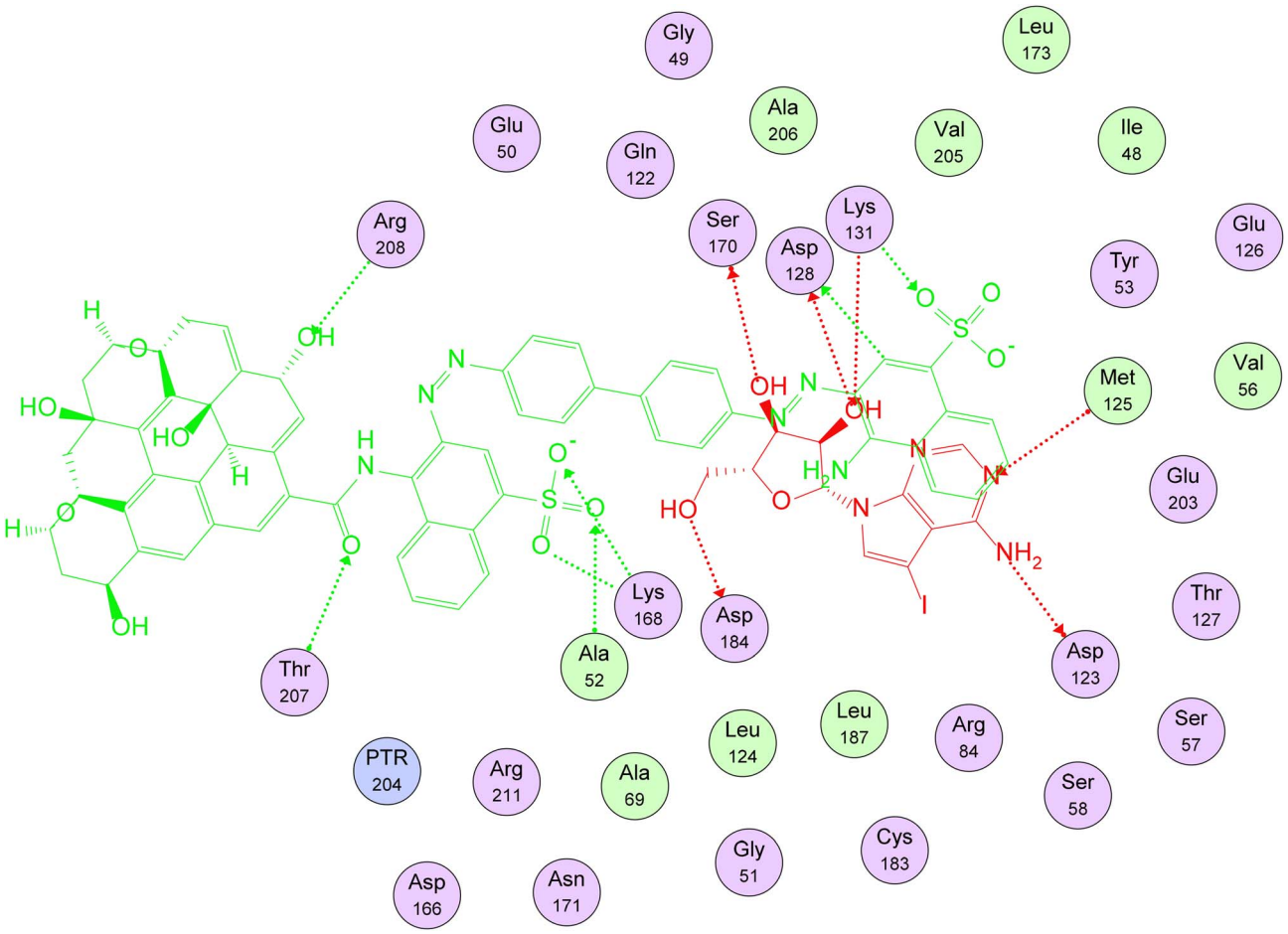

Fig. 28 A 2D-visualization showing the alignment of the GO and the co-crystallized inhibitor in the pocket of the active site of 2ZOQ.

established multiple hydrogen-bond acceptor interactions, including those between atom N16 and MET125 (2.92 Å), O59 and ASN171 (2.68 Å), and O60 and LYS181 (2.85 Å), each contributing favorably to the overall binding stability, with interaction energies ranging from −0.8 to −2.3 kcal mol^{-1}. In addition to these hydrogen bonds, the ligand formed notable ionic interactions, particularly with LYS168 through atoms O58 and O59 at distances of 3.51 Å and 3.16 Å, respectively, with the latter showing a strong interaction energy of −3.5 kcal mol^{-1}. Further ionic contact was observed between O60 and LYS181 (3.89 Å), contributing additional stabilization. Collectively, these hydrogen-bonding and ionic interactions highlight the strong electrostatic complementarity between the ligand and the active-site residues, supporting the predicted affinity inferred from the docking results.

Overall, the docking results suggest that Congo red exhibits a strong and stable binding mode within the 2ZOQ active site, supported by favorable energy scores and hydrogen-bond and ionic interactions. These findings indicate that Congo red has the potential to interact effectively with 2ZOQ and may serve as a promising scaffold for the development of CD45-targeting inhibitory systems.

6.3.4. Molecular docking of rGO. Docking simulations of rGO (small sector of GM) with the 2ZOQ revealed a stable and well-defined binding pose within the active-site cavity. As shown in Fig. 24, the rGO fragment adopted a conformation that fits appropriately within the catalytic pocket, demonstrating favorable steric compatibility with the receptor surface. Despite its extended aromatic structure and polar oxygen surface functionalities, rGO was able to assume a stable orientation that allowed effective interactions with key residues of the binding site.

Superposition of the rGO docked pose with the co-crystallized inhibitor further confirmed the reliability of the predicted binding mode. As illustrated in Fig. 25, rGO aligns within the active-site region in a manner highly consistent with the reference ligand, demonstrating strong spatial agreement between the two structures. This alignment is quantitatively supported by the acceptable RMSD value of the selected pose (1.99 Å), which indicates a high degree of structural similarity and reinforces the validity of the docking results.

The docked ligand displayed a strong and energetically favorable binding profile, as reflected by its docking score of −19.29 kcal mol^{-1}. Detailed interaction analysis illustrated in Fig. 26 revealed a network of stabilizing contacts within the active site, including several hydrogen–donor interactions with CYS183 (C8, O47, O53) and a key H–donor bond between O57 and ASP184. Notably, interaction with ASP184 is highly

significant because this residue also forms a hydrogen bond with the co-crystallized ligand, highlighting its central role in ligand recognition and active-site stabilization. The ligand further engaged in strong hydrogen–acceptor interactions with LYS131 (O45, 2.56 Å, −5.5 kcal mol^{-1}) and GLN122, with the LYS131 interaction being particularly important, as it is likewise conserved in the binding mode of the reference inhibitor. This conservation of interactions with ASP184 and LYS131 strengthens confidence in the predicted binding pose and supports its biological relevance. Additionally, a π–H interaction between the aromatic ring and VAL56 contributed supplementary hydrophobic stabilization. Together, these interactions demonstrate that the ligand binds in a manner consistent with essential active-site features, reinforcing the validity of the docking results.

Although the overall binding affinity of rGO is lower than that of Congo red, its ability to form multiple stabilizing interactions and penetrate the active-site cavity supports the potential relevance of graphene-based structures in modulating the 2ZOQ function.

6.3.5. Molecular docking of GC. Docking analysis of the GC (small sector of GCM) against the 2ZOQ active site demonstrated a highly stable and energetically favorable binding configuration. The conjugate accommodated the catalytic pocket with a strong steric complementarity and appropriate orientation toward key catalytic residues, as shown in Fig. 27. The calculated docking score of −22.92 kcal mol^{-1} indicates a remarkably high binding affinity when compared to the native ligand and individual components, suggesting a synergistic enhancement in interaction strength upon conjugation.

Superposition of the GC docked pose with the co-crystallized inhibitor further confirmed the reliability of the predicted binding mode. As illustrated in Fig. 28, GC aligns within the active site region in a manner closely consistent with the reference ligand, demonstrating strong spatial agreement between the two structures. This structural overlap is quantitatively supported by the RMSD value of the selected pose (1.48 Å), which falls well within the accepted threshold for reliable docking and indicates that both ligands occupy highly similar positions within the active site.

The binding stability of the GC–protein complex is reinforced by a network of intermolecular interactions distributed across key catalytic residues within the active site (Fig. 29). The ligand forms multiple hydrogen-bonding interactions, including H–donor contact with ASP128 (3.43 Å, −0.8 kcal mol^{-1}), and several H–acceptor interactions with residues, such as ARG208 (3.38 Å and 3.11 Å, −0.6 and −2.0 kcal mol^{-1}), LYS131 (3.41 Å, −1.3 kcal mol^{-1}), ALA52 (2.83 Å, −4.2 kcal mol^{-1}), LYS168 (3.19 Å, −1.4 kcal mol^{-1}), and THR207 (3.39 Å, −0.7 kcal mol^{-1}). In addition to hydrogen bonding, strong ionic interactions were detected with positively charged residues, particularly LYS131 (−2.2 kcal mol^{-1}) and two contacts with LYS168 (2.85 Å and 3.19 Å, −5.6 and −3.3 kcal mol^{-1}), indicating substantial electrostatic

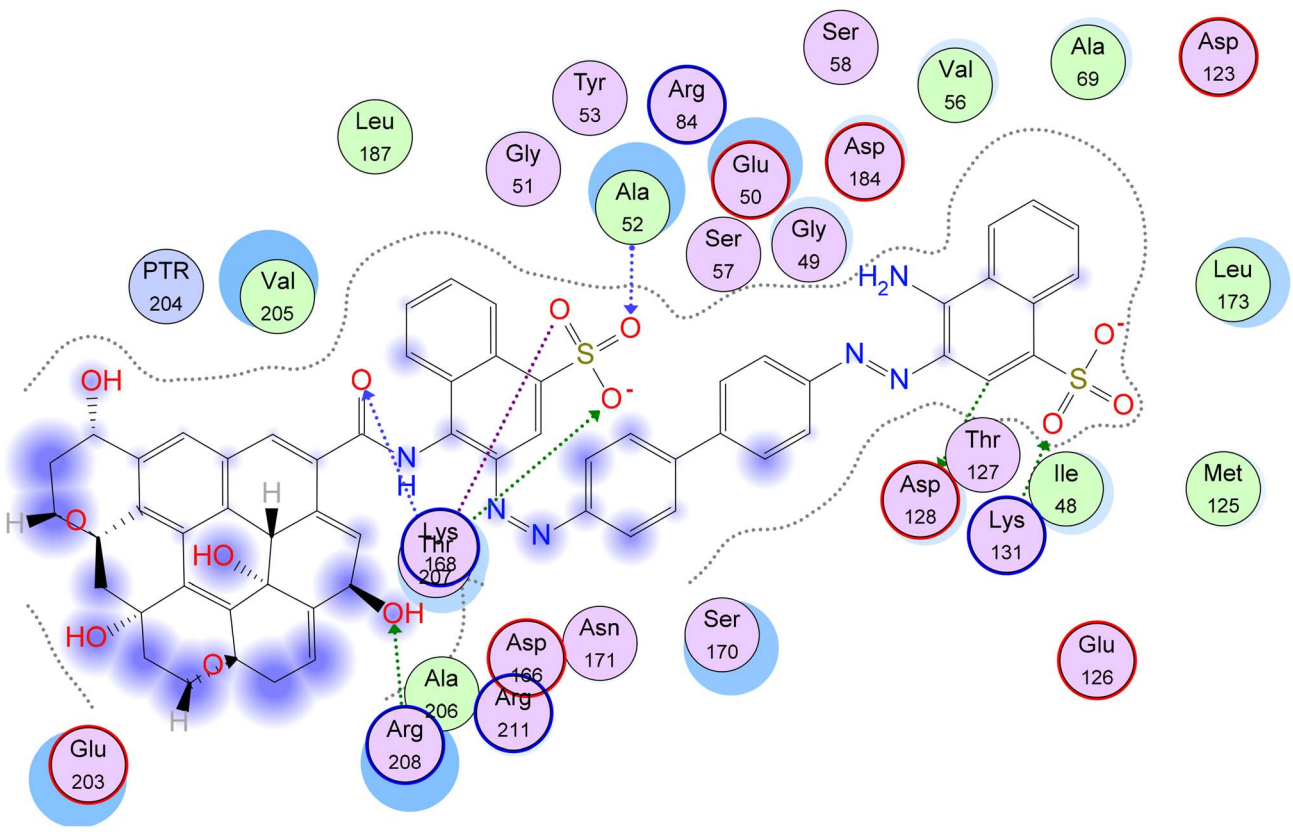

Fig. 29 2D depiction showing the binding modes of the graphene oxide–Congo red conjugate in the 2ZOQ protein active site.

stabilization. Collectively, these interactions—especially those involving ASP128, LYS131, and LYS168—underscore the robust anchoring of the ligand within the active site and contribute to the overall stability and affinity of the docked complex.

The combination of these interactions creates a robust binding network spanning essential residues, including ASP128, ARG208, LYS131, ALA52, LYS168, and THR207, with ASP128 and LYS131 key residues being functionally critical within the 2ZOQ catalytic domain. These residues collectively provide hydrogen-bonding, ionic stabilization, and polar contacts that firmly anchor the conjugate within the active-site pocket. The distribution and strength of these stabilizing interactions highlight the high affinity of the conjugate for 2ZOQ, emphasizing its potential as a potent inhibitor. Overall, the conjugate not only fits favorably within the active-site cavity but also establishes an extensive and energetically significant interaction network, indicating substantial biological relevance and promising inhibitory capability.

7 Conclusion

For the first time, rGO was covalently functionalized with Congo red molecules *via* amidation coupling, followed by noncovalent combination with barium ferrite nanoparticles (GCM), as tumor suppressor agents against breast and colon cancers. GCM was compared with rGO–barium ferrite nanoparticles (GM) that were synthesized with a one-pot *in situ* sol–gel method, GO–CONH–Congo red molecules (GC), and the pure reagents GO and barium ferrite nanoparticles (M). Various physicochemical characterization methods were applied to identify the synthesized nanomaterials, including IR, XRD, UV-Vis spectroscopy, TGA, SEM, EDX, TEM, VSM, size distribution, and ζ-potentials. The results showed the successful formation of amide bonds between the GO surface and the Congo red molecules using EDC/NHS coupling, and the surface of GO was reduced to rGO during the synthesis of GCM and GM. Barium ferrite nanoparticles were synthesized using the sol–gel auto-combustion method, and SEM pictures showed the spread of M on GCM and GM surfaces and also inside the voids, M_s values for M (59 emu g^{-1}) > GCM (35 emu g^{-1}) > GM (25 emu g^{-1}), the decrease in saturation magnetization can be ascribed to the presence of random spin orientation as a result of graphene domains that have surface defects and cavities produced during the synthesis process. M, GCM, and GM exhibit coercivity values of 2183 Oe, 212 Oe, and 147 Oe, respectively, which confirm the hard magnetic properties of M and the soft magnetic character of GCM and GM.

MTT assays demonstrated that both GM and GCM exhibit potent and selective anti-proliferative activity against human colon and breast cancer cell replication without affecting normal cells. Safe action was observed for pure Congo red molecules on all cancer cells, while the magnetic graphene structures involved in GM and GCM demonstrated efficient inhibition for the growth of both types of cancer cells. This confirms the role of ferrite nanoparticles loaded on graphene substrates as antiproliferative agents against replication of cancer cells by catalyzing Fenton-like reactions activity inside the H_2O_2-rich cancer cell microenvironment, leading to oxidative stress and ferroptosis. This reactivity is enhanced by the ferrite particle size and the concentration of H_2O_2 inside the cancer cells and can explain the observed variation in cytotoxic activity of M, which is potent against MCF-7 (IC_{50} = 16 μg mL^{-1}), moderate against HCT116 (IC_{50} = 53 μg mL^{-1}) and non-toxic to normal Vero cells (IC_{50} > 100 μg mL^{-1}).

Molecular studies confirmed that the cytotoxicity of GC and GCM is exerted through a mechanism of severe DNA damage, culminating in intrinsic caspase-dependent apoptosis. To advance these compounds toward clinical relevance, essential *in vivo* investigations are now warranted.

To optimize the molecular design of such materials for application in cancer theranostics, the Congo red molecules covalently attached to the graphene surface can enhance the material specificity for cancer cells, without affecting the normal cells, by binding to the β-sheet amyloid-like aggregates of mutant p53 that are intensified in cancer cell microenvironments. The high surface area of graphene sheets, which contain various voids capable of encapsulating ferrite nanoparticles, helps preserve their uniform distribution on the graphene substrate and enhances catalytic activity in Fenton reactions. Additionally, functionalization of the graphene surface and the reduction in particle size of magnetic ferrite nanoparticles – achieved by optimizing synthesis conditions – resulted in soft magnetic properties, smaller ferrite particle sizes were obtained on GCM (≈11 nm) and GM (≈21 nm) compared to M (≈66 nm). These properties qualify the designed magnetic graphene nanomaterials, especially GCM, as smart theranostics nanorobots that can be externally controlled by a magnetic field. The soft magnetic properties facilitate magnetization and demagnetization of its surface, preventing the accumulation of the magnetic nanoparticles after removal of magnetism, and reducing the cytotoxicity that can accompany the residual magnetism, allowing enhanced magnetic hyperthermia, bioimaging, targeted drug delivery, biosensors, and theranostics applications. Molecular docking studies demonstrated that the GC sectors confirmed the highest docking score (−22.92 kcal mol^{-1}), indicating a synergistic improvement in binding affinity upon conjugation, and possible interference with CD45-regulated signaling pathways that can contribute to the observed anticancer effects.

Ethics approval and consent to participate

All co-authors confirm their participation in this manuscript and that it has not been published previously; it is not under consideration for publication elsewhere. We conducted experiments using only cell lines; our study did not involve any human tissue.

Consent for publication

All co-authors approve the manuscript for publication in the *Journal of Scientific Reports*.

Author contributions

All authors contributed to the conception and design of the study. Material preparation, data collection and analysis were performed by Abdelsattar O. E. Abdelhalim, Nasra F Abdel Fattah, Mohamed Z. Hussein, Mangoud M. Mangoud, and Samah A Loutfy. The first draft of the manuscript was written by Abdelsattar O. E. Abdelhalim and all authors commented on previous versions of the manuscript. All authors read and approved the final manuscript.

Conflicts of interest

All listed authors of this manuscript declare that they have no conflicts of interest.

Data availability

Data sets generated during the current study cannot be shared openly but are available from the corresponding author on reasonable request.

Abbreviations

MTT	3-(4,5-Dimethylthiazol-2-yl)-2,5-diphenyltetrazolium bromide
HCT116	Human colon cancer cells
MCF-7	Human breast cancer cells
GO	Graphene oxide
rGO	Reduced graphene oxide
A549	Human lung cancer cell line
HEK293	Human embryonic kidney cell line
XRD	X-ray diffraction
TGA	Thermogravimetric analysis
SEM	Scanning electron microscopy
EDX	Energy dispersive X-ray spectroscopy
HRTEM	High-resolution transmission electron microscopy
VSM	Vibrating sample magnetometer
EDC	1-Ethyl-3-(3-dimethylaminopropyl) carbodiimide
NHS	*N*-Hydroxysuccinimide
DMEM	Dulbecco's Modified Eagle Medium
GC	Graphene oxide functionalized with Congo red molecules
M	Barium ferrite magnetic nanoparticles
GCM	Reduced graphene oxide functionalized with Congo red molecules and barium ferrite nanoparticles
GM	Reduced graphene oxide functionalized with barium ferrite nanoparticles
qRT-PCR	Quantitative real-time PCR
C	Congo red molecules

Acknowledgements

The authors acknowledge the National Center for Social and Criminological Research, 4 Agouza, Giza, 11561, Egypt, for registering the scientific plan of this research in the Environmental Research Department at the Chemical and Biological Research Division. Research was performed using the equipment of the Virology and Immunology Unit, Cancer Biology Department, National Cancer Institute, Cairo University; the Central Laboratories at the National Research Center; and the Micro Analytical Center, Faculty of Science, Cairo University. The work was supported with chemicals, analysis, and devices by the National Center for Social and Criminological Research.

References

1 H. Yu and W. Feng, Carbon-Based Multifunctional Nanomaterials, *Nanomaterials*, 2024, **14**, 1600, DOI: 10.3390/NANO14191600.

2 H. Maulina, E. Widianto, E. Subama, M. Riswan, C. Driyo, D. N. Rositawati, F. Nugroho, M. E. Wibowo and I. Santoso, Optical properties of CVD-grown multilayer graphene on nickel using spectroscopic ellipsometry, *Opt. Mater.*, 2024, **157**, 116300, DOI: 10.1016/J.OPTMAT.2024.116300.

3 M. S. K. Chowdury, Y. J. Park, S. B. Park and Y. il Park, Review: Two-dimensional nanostructured pristine graphene and heteroatom-doped graphene-based materials for energy conversion and storage devices, *Sustain. Mater. Technol.*, 2024, **42**, e01124, DOI: 10.1016/J.SUSMAT.2024.E01124.

4 V. Dutta, P. Singh, P. Shandilya, S. Sharma, P. Raizada, A. K. Saini, V. K. Gupta, A. Hosseini-Bandegharaei, S. Agarwal and A. Rahmani-Sani, Review on advances in photocatalytic water disinfection utilizing graphene and graphene derivatives-based nanocomposites, *J. Environ. Chem. Eng.*, 2019, **7**, 103132, DOI: 10.1016/J.JECE.2019.103132.

5 A. Darmawan, H. Zakiyah, H. Muhtar and M. Elma, Graphene oxide/silicon dioxide (GO/SiO2) hybrid coating on zirconia ceramic for sustainable water desalination, *Ceram. Int.*, 2024, **50**, 47232–47243, DOI: 10.1016/J.CERAMINT.2024.09.074.

6 P. Cui, Z. Li, Q. Wu and X. Hou, Optoelectronic properties and charge transfer dynamics in graphene quantum dot/Ir(III) nanocomposites: Enhancing photocatalytic performance through strategic BTF conjugate binding and end-capping variations, *Diamond Relat. Mater.*, 2024, **145**, 111107, DOI: 10.1016/J.DIAMOND.2024.111107.

7 Y. Qu, F. He, C. Yu, X. Liang, D. Liang, L. Ma, Q. Zhang, J. Lv and J. Wu, Advances on graphene-based nanomaterials for biomedical applications, *Mater. Sci. Eng., C*, 2018, **90**, 764–780, DOI: 10.1016/J.MSEC.2018.05.018.

8 A. H. Mashhadzadeh, A. H. Mashhadzadeh, B. Golman, C. Spitas, S. A. Faroughi and K. V. Kostas, Recent Advancements in Mechanical Properties of Graphene-Enhanced Polymer Nanocomposites: Progress, Challenges, and Pathways Forward, *J. Mol. Graph. Model.*, 2024, 108908, DOI: 10.1016/J.JMGM.2024.108908.

9 J. H. Jeong, S. Kang, N. Kim, R. Joshi and G. H. Lee, Recent trends in covalent functionalization of 2D materials, *Phys.*

Chem. Chem. Phys., 2022, **24**, 10684–10711, DOI: 10.1039/D1CP04831G.

10 L. Basta, A. Moscardini, F. Fabbri, L. Bellucci, V. Tozzini, S. Rubini, A. Griesi, M. Gemmi, S. Heun and S. Veronesi, Covalent organic functionalization of graphene nanosheets and reduced graphene oxide via 1,3-dipolar cycloaddition of azomethine ylide, *Nanoscale Adv.*, 2021, **3**, 5841–5852, DOI: 10.1039/D1NA00335F.

11 J. Narayan and K. Bezborah, Recent advances in the functionalization, substitutional doping and applications of graphene/graphene composite nanomaterials, *RSC Adv.*, 2024, **14**, 13413–13444, DOI: 10.1039/D3RA07072G.

12 F. K. F. dos Santos, A. A. M. P. Júnior, A. L. N. Filho, C. J. N. Fonseca, D. K. M. Isidorio, F. de A. Araújo, P. H. A. Oliveira and V. F. da Veiga Júnior, Graphene and Natural Products: A Review of Antioxidant Properties in Graphene Oxide Reduction, *Int. J. Mol. Sci.*, 2024, **25**(10), 5182, DOI: 10.3390/IJMS25105182.

13 A. D. Sontakke, S. Tiwari and M. K. Purkait, A comprehensive review on graphene oxide-based nanocarriers: Synthesis, functionalization and biomedical applications, *FlatChem*, 2023, **38**, 100484, DOI: 10.1016/J.FLATC.2023.100484.

14 K. Vinothini, S. S. Dhilip Kumar, H. Abrahamse and M. Rajan, Synergistic effect of polymer functionalized graphene oxide system for breast cancer treatment, *Int. J. Pharm.*, 2023, **632**, 122556, DOI: 10.1016/j.ijpharm.2022.122556.

15 M. Haider, R. Cagliani, J. Jagal, M. N. Jayakumar, B. Fayed, S. B. Shakartalla, R. Pasricha, K. Greish and R. El-Awady, Peptide-functionalized graphene oxide quantum dots as colorectal cancer theranostics, *J. Colloid Interface Sci.*, 2023, **630**, 698–713, DOI: 10.1016/j.jcis.2022.10.045.

16 D. S. G and M. B, A comprehensive review on current trends in greener and sustainable synthesis of ferrite nanoparticles and their promising applications, *Results Eng.*, 2024, **21**, 101702, DOI: 10.1016/J.RINENG.2023.101702.

17 S. Kohzadi, N. Najmoddin, H. Baharifar and M. Shabani, Functionalized SPION immobilized on graphene-oxide: Anticancer and antiviral study, *Diamond Relat. Mater.*, 2022, **127**, 109149, DOI: 10.1016/J.DIAMOND.2022.109149.

18 A. Espargaró, S. Llabrés, S. J. Saupe, C. Curutchet, F. J. Luque and R. Sabaté, On the Binding of Congo Red to Amyloid Fibrils, *Angew. Chem., Int. Ed.*, 2020, **59**, 8104–8107, DOI: 10.1002/ANIE.201916630.

19 P. Frid, S. V. Anisimov and N. Popovic, Congo red and protein aggregation in neurodegenerative diseases, *Brain Res. Rev.*, 2007, **53**, 135–160, DOI: 10.1016/J.BRAINRESREV.2006.08.001.

20 D. B. Carter and K. C. Chou, A model for structure-dependent binding of Congo red to Alzheimer β-amyloid fibrils, *Neurobiol. Aging*, 1998, **19**, 37–40, DOI: 10.1016/S0197-4580(97)00164-4.

21 W. E. Klunk, J. W. Pettegrew and D. J. Abraham, Quantitative evaluation of congo red binding to amyloid-like proteins with a beta-pleated sheet conformation, *J. Histochem. Cytochem.*, 1989, **37**, 1273–1281, DOI: 10.1177/37.8.2666510.

22 A. A. Reinke and J. E. Gestwicki, Insight into Amyloid Structure Using Chemical Probes, *Chem. Biol. Drug Des.*, 2011, **77**, 399, DOI: 10.1111/J.1747-0285.2011.01110.X.

23 A. J. Howie, D. B. Brewer, D. Howell and A. P. Jones, Physical basis of colors seen in Congo red-stained amyloid in polarized light, *Lab. Invest.*, 2008, **88**, 232–242, DOI: 10.1038/LABINVEST.3700714.

24 A. Zayas-Santiago, A. Díaz-García, R. Nuñez-Rodríguez and M. Inyushin, Accumulation of amyloid beta in human glioblastomas, *Clin. Exp. Immunol.*, 2020, **202**, 325–334, DOI: 10.1111/CEI.13493.

25 D. N. Nguyen, A. Qureshi, M. A. Salvian, P. Xiao and C. Chen, Amyloidosis Found in the Breast: A Case Report, *Am. J. Case Rep.*, 2024, **25**, e944755, DOI: 10.12659/AJCR.944755.

26 A. P. D. Ano Bom, L. P. Rangel, D. C. F. Costa, G. A. P. De Oliveira, D. Sanches, C. A. Braga, L. M. Gava, C. H. I. Ramos, A. O. T. Cepeda, A. C. Stumbo, C. V. De Moura Gallo, Y. Cordeiros and J. L. Silva, Mutant p53 Aggregates into Prion-like Amyloid Oligomers and Fibrils: IMPLICATIONS FOR CANCER, *J. Biol. Chem.*, 2012, **287**, 28152–28162, DOI: 10.1074/JBC.M112.340638.

27 J. L. Silva, C. V. D. M. Gallo, D. C. F. Costa and L. P. Rangel, Prion-like aggregation of mutant p53 in cancer, *Trends Biochem. Sci.*, 2014, **39**, 260–267, DOI: 10.1016/j.tibs.2014.04.001.

28 C. B. Levy, A. C. Stumbo, A. P. D. Ano Bom, E. A. Portari, Y. Carneiro, J. L. Silva and C. V. De Moura-Gallo, Co-localization of mutant p53 and amyloid-like protein aggregates in breast tumors, *Int. J. Biochem. Cell Biol.*, 2011, **43**, 60–64, DOI: 10.1016/j.biocel.2010.10.017.

29 J. L. Silva, E. A. Cino, I. N. Soares, V. F. Ferreira and G. De Oliveira, Targeting the Prion-like Aggregation of Mutant p53 to Combat Cancer, *Acc. Chem. Res.*, 2018, **51**, 181–190, DOI: 10.1021/ACS.ACCOUNTS.7B00473.

30 A. Soragni, D. M. Janzen, L. M. Johnson, A. G. Lindgren, A. Thai-Quynh Nguyen, E. Tiourin, A. B. Soriaga, J. Lu, L. Jiang, K. F. Faull, M. Pellegrini, S. Memarzadeh and D. S. Eisenberg, A Designed Inhibitor of p53 Aggregation Rescues p53 Tumor Suppression in Ovarian Carcinomas, *Cancer Cell*, 2016, **29**, 90–103, DOI: 10.1016/J.CCELL.2015.12.002.

31 J. Zhao, C. Feng, F. Zheng, Y. Qian, X. Zhang and H. Wang, Electron Density Modulation-Enhanced Magnetic Nanocatalysis for Anti-Tumor Therapy, *Adv. Funct. Mater.*, 2025, **35**, 2422270, DOI: 10.1002/ADFM.202422270.

32 Chemical Computing Group (CCG), Computer-Aided Molecular Design, https://www.chemcomp.com/en/index.htm, accessed on December 3, 2025.

33 A. Adetayo and D. Runsewe, Synthesis and Fabrication of Graphene and Graphene Oxide: A Review, *Open J. Compos. Mater.*, 2019, **09**, 207–229, DOI: 10.4236/ojcm.2019.92012.

34 T. Charoensuk, W. Thongsamrit, C. Ruttanapun, P. Jantaratana and C. Sirisathitkul, Loading Effect of Sol-Gel Derived Barium Hexaferrite on Magnetic Polymer Composites, *Nanomaterials*, 2021, **11**, 558, DOI: 10.3390/NANO11030558.

35 G. H. Elgemeie, M. A. Abu-Zaied and S. A. Loutfy, 4-Aminoantipyrine in carbohydrate research: Design, synthesis and anticancer activity of thioglycosides of a novel class of 4-aminoantipyrines and their corresponding pyrazolopyrimidine and pyrazolopyridine thioglycosides, *Tetrahedron*, 2017, **73**, 5853–5861, DOI: 10.1016/j.tet.2017.08.024.

36 T. Mosmann, Rapid colorimetric assay for cellular growth and survival: Application to proliferation and cytotoxicity assays, *J. Immunol. Methods*, 1983, **65**, 55–63, DOI: 10.1016/0022-1759(83)90303-4.

37 S. A. Loutfy, M. H. Elberry, K. Y. Farroh, H. T. Mohamed, A. A. Mohamed, E. B. Mohamed, A. H. I. Faraag and S. A. Mousa, Antiviral activity of chitosan nanoparticles encapsulating curcumin against hepatitis C virus genotype 4a in human hepatoma cell lines, *Int. J. Nanomed.*, 2020, **15**, 2699–2715, DOI: 10.2147/IJN.S241702.

38 S. A. Loutfy, H. M. A. El-Din, M. H. Elberry, N. G. Allam, M. T. M. Hasanin and A. M. Abdellah, Synthesis, characterization and cytotoxic evaluation of chitosan nanoparticles: In vitro liver cancer model, *Adv. Nat. Sci. Nanosci. Nanotechnol.*, 2016, **7**, 035008, DOI: 10.1088/2043-6262/7/3/035008.

39 T. D. Schmittgen and K. J. Livak, Analyzing real-time PCR data by the comparative CT method, *Nat. Protoc.*, 2008, **3**, 1101–1108, DOI: 10.1038/nprot.2008.73.

40 Index-Calcnet-TargetNet, http://targetnet.scbdd.com/calcnet/index/, accessed on December 3, 2025.

41 Index-Home-TargetNet, http://targetnet.scbdd.com/, accessed on December 3, 2025.

42 H. M. Berman, J. Westbrook, Z. Feng, G. Gilliland, T. N. Bhat, H. Weissig, I. N. Shindyalov and P. E. Bourne, The Protein Data Bank, *Nucleic Acids Res.*, 2000, **28**, 235–242, DOI: 10.1093/NAR/28.1.235.

43 B. Das, H. Meirovitch and I. M. Navon, Performance of hybrid methods for large-scale unconstrained optimization as applied to models of proteins, *J. Comput. Chem.*, 2003, **24**, 1222–1231, DOI: 10.1002/JCC.10275.

44 R. M. Abdallah, Extending Chemoinformatics Techniques With JMolecular Energy: A Robust CDK-Based Force Field Library, *J. Comput. Chem.*, 2025, **46**(6), e70071, DOI: 10.1002/JCC.70071.

45 R. Ghorbanpour Ghartavool, G. R. Gordani, M. R. Loghman Estarki, M. Tavoosi, M. Mazaheri Forushani and E. Kiani, Synthesis, microstructure, magnetic and electromagnetic behavior of graphene oxide/hexagonal barium ferrite aerogel nanocomposites within the frequency range of 1–18 GHz, *Arab. J. Chem.*, 2023, **16**, 105099, DOI: 10.1016/J.ARABJC.2023.105099.

46 N. V. Chukanov, *Infrared spectra of mineral species*, 2014, DOI: 10.1007/978-94-007-7128-4.

47 P. K. Ravichandran and C. Munusamy, Optimization of reduced Graphene oxide synthesis using central composite design analysis-A waste to value approach, *Environ. Sci. Pollut. Res. Int.*, 2023, **30**, 28259–28273, DOI: 10.1007/S11356-022-24018-0.

48 J. Yao, A. Guan, W. Ruan and Y. Ma, In Situ Preparation of rGO-Cement Using Thermal Reduction Method and Performance Study, *Materials*, 2024, **17**, 1209, DOI: 10.3390/MA17051209.

49 N. Salidkul, W. Mongkolthanaruk, K. Faungnawakij and S. Pinitsoontorn, Hard magnetic membrane based on bacterial cellulose – Barium ferrite nanocomposites, *Carbohydr. Polym.*, 2021, **264**, 118016, DOI: 10.1016/J.CARBPOL.2021.118016.

50 B. C. Brightlin and S. Balamurugan, The effect of post annealing treatment on the citrate sol–gel derived nanocrystalline BaFe12O19 powder: structural, morphological, optical and magnetic properties, *Appl. Nanosci.*, 2016, **6**, 1199–1210, DOI: 10.1007/S13204-016-0531-1/TABLES/3.

51 U. A. Méndez-Romero, S. A. Pérez-García, Q. Fan, E. Wang and L. Licea-Jiménez, Lateral size reduction of graphene oxide preserving its electronic properties and chemical functionality, *RSC Adv.*, 2020, **10**, 29432–29440, DOI: 10.1039/D0RA04726K.

52 S. Gurunathan, J. W. Han, A. Abdal Dayem, V. Eppakayala and J. H. Kim, Oxidative stress-mediated antibacterial activity of graphene oxide and reduced graphene oxide in Pseudomonas aeruginosa, *Int. J. Nanomed.*, 2012, **7**, 5901–5914, DOI: 10.2147/IJN.S37397.

53 H. Zhu, R. Jiang, L. Xiao, Y. Chang, Y. Guan, X. Li and G. Zeng, Photocatalytic decolorization and degradation of Congo Red on innovative crosslinked chitosan/nano-CdS composite catalyst under visible light irradiation, *J. Hazard. Mater.*, 2009, **169**, 933–940, DOI: 10.1016/J.JHAZMAT.2009.04.037.

54 K. Habanjar, H. Shehabi, A. M. Abdallah and R. Awad, Effect of calcination temperature and cobalt addition on structural, optical and magnetic properties of barium hexaferrite BaFe12O19 nanoparticles, *Appl. Phys. A Mater. Sci. Process.*, 2020, **126**, 1–11, DOI: 10.1007/S00339-020-03497-3.

55 M. K. Rabchinskii, V. V. Shnitov, A. T. Dideikin, A. E. Aleksenskii, S. P. Vul, M. V. Baidakova, I. I. Pronin, D. A. Kirilenko, P. N. Brunkov, J. Weise and S. L. Molodtsov, Nanoscale perforation of graphene oxide during photoreduction process in the argon atmosphere, *J. Phys. Chem. C*, 2016, **120**, 28261–28269, DOI: 10.1021/ACS.JPCC.6B08758.

56 S. Yang, W. Yue, D. Huang, C. Chen, H. Lin and X. Yang, A facile green strategy for rapid reduction of graphene oxide by metallic zinc, *RSC Adv.*, 2012, **2**, 8827–8832, DOI: 10.1039/C2RA20746J.

57 Y. Zhang, W. Hu, B. Li, C. Peng, C. Fan and Q. Huang, Synthesis of polymer-protected graphene by solvent-assisted thermal reductionprocess, *Nanotechnology*, 2011, **22**, 345601, DOI: 10.1088/0957-4484/22/34/345601.

58 W. Li, U. W. Gedde, H. Hillborg, Electric Field Grading Material Based on Thermally Reduced Graphene Oxide, in *Proceedings of the Nordic Insulation Symposium*, 2017, DOI: 10.5324/NORDIS.V0I24.2282.

59 G. Packiaraj, M. Hashim, K. Chandra Babu Naidu, G. Helen Ruth Joice, J. L. Naik, D. Ravinder and B. Ramakrishna Rao, Magnetic properties of Cu and Al doped nano BaFe12O19 ceramics, *Biointerface Res. Appl. Chem.*, 2020, **10**, 5455–5459, DOI: 10.33263/BRIAC103.455459.

60 T. Kim and M. Shima, Reduced magnetization in magnetic oxide nanoparticles, *J. Appl. Phys.*, 2007, **101**, 09M516, DOI: 10.1063/1.2712825.

61 N. Ullah Khan, N. Amin, M. Uzair Khalid, M. Amami and M. Ajaz un Nabi, Tailoring the structural, electrical, dielectric, and magnetic properties of graphene nanoplatelets (GNPs)-incorporated Ni0.35Zn0.25Cd0.4Fe2O4 ferrite composites, *Mater. Sci. Eng., B*, 2024, **308**, 117580, DOI: 10.1016/J.MSEB.2024.117580.

62 T. Zhao, W. Jin, Y. Wang, X. Ji, H. Yan, C. Xiong, X. Lou, A. Dang, H. Li and T. Li, In situ synthesis and electromagnetic wave absorbing properties of sandwich microstructured graphene/La-doped barium ferrite nanocomposite, *RSC Adv.*, 2017, **7**, 37276–37285, DOI: 10.1039/C7RA06716J.

63 M. Sepioni, R. R. Nair, S. Rablen, J. Narayanan, F. Tuna, R. Winpenny, A. K. Geim and I. V. Grigorieva, Limits on intrinsic magnetism in graphene, *Phys. Rev. Lett.*, 2010, **105**, 207205, DOI: 10.1103/PhysRevLett.105.207205.

64 M. D. Nurhafizah, Magnetic properties of graphene oxide via a simple mixing with waste engine oil-based carbon nanotubes, *SN Appl. Sci.*, 2020, **2**, 1–6, DOI: 10.1007/S42452-020-2361-8.

65 Z. Li, L. Chen, S. Meng, L. Guo, J. Huang, Y. Liu, W. Wang and X. Chen, Field and temperature dependence of intrinsic diamagnetism in graphene: Theory and experiment, *Phys. Rev. B*, 2015, **91**, 094429, DOI: 10.1103/PhysRevB.91.094429.

66 V. Shukla, Observation of critical magnetic behavior in 2D carbon based composites, *Nanoscale Adv.*, 2020, **2**, 962, DOI: 10.1039/C9NA00663J.

67 M. Koleoso, X. Feng, Y. Xue, Q. Li, T. Munshi and X. Chen, Micro/nanoscale magnetic robots for biomedical applications, *Mater. Today Bio*, 2020, **8**, 100085, DOI: 10.1016/J.MTBIO.2020.100085.

68 H. Zhou, C. C. Mayorga-Martinez, S. Pané, L. Zhang and M. Pumera, Magnetically Driven Micro and Nanorobots, *Chem. Rev.*, 2021, **121**, 4999–5041, DOI: 10.1021/ACS.CHEMREV.0C01234.

69 F. Liu, X. Liu, Q. Huang, and T. Arai, Recent Progress of Magnetically Actuated DNA Micro/Nanorobots, in *Cyborg and Bionic Systems 2022*, 2022, DOI: 10.34133/2022/9758460.

70 N. Hu, L. Ding, Y. Liu, K. Wang, B. Zhang, R. Yin, W. Zhou, Z. Bi and W. Zhang, Development of 3D-Printed Magnetic Micro-Nanorobots for Targeted Therapeutics: the State of Art, *Adv. NanoBiomed Res.*, 2023, **3**, 2300018, DOI: 10.1002/ANBR.202300018.

71 T. Kong, Q. Zheng, J. Sun, C. Wang, H. Liu, Z. Gao, Z. Qiao, W. Yang, T. Kong, Q. Zheng, J. Sun, C. Wang, H. Liu, Z. Gao, Z. Qiao and W. Yang, Advances in Magnetically Controlled Medical Robotics: A Review of Actuation Systems, Continuum Designs, and Clinical Prospects for Minimally Invasive Therapies, *Micromachines*, 2025, **16**, 16, DOI: 10.3390/MI16050561.

72 H. Shen, S. Cai, Z. Wang, Z. Ge and W. Yang, Magnetically driven microrobots: Recent progress and future development, *Mater. Des.*, 2023, **227**, 111735, DOI: 10.1016/J.MATDES.2023.111735.

73 A. L. Costa, A. C. Gomes, M. Pillinger, I. S. Gonçalves, J. Pina and J. S. Seixas de Melo, Insights into the Photophysics and Supramolecular Organization of Congo Red in Solution and the Solid State, *ChemPhysChem*, 2017, **18**, 564–575, DOI: 10.1002/CPHC.201601236.

74 M. Awashra and P. Młynarz, The toxicity of nanoparticles and their interaction with cells: an in vitro metabolomic perspective, *Nanoscale Adv.*, 2023, **5**, 2674–2723, DOI: 10.1039/d2na00534d.

75 D. Zahn, M. Diegel, A. Valitova, J. Dellith and S. Dutz, Magnetic Barium Hexaferrite Nanoparticles with Tunable Coercivity as Potential Magnetic Heating Agents, *Nanomaterials*, 2024, **14**, 992, DOI: 10.3390/NANO14120992.

76 M. Yusefi, K. Shameli, H. Jahangirian, S. Y. Teow, L. Afsah-Hejri, S. N. A. Mohamad Sukri and K. Kuča, How Magnetic Composites are Effective Anticancer Therapeutics? A Comprehensive Review of the Literature, *Int. J. Nanomed.*, 2023, **18**, 3535, DOI: 10.2147/IJN.S375964.

77 T. Ali, D. Li, T. N. F. Ponnamperumage, A. K. Peterson, J. Pandey, K. Fatima, J. Brzezinski, J. A. R. Jakusz, H. Gao, G. E. Koelsch, D. S. Murugan and X. Peng, Generation of Hydrogen Peroxide in Cancer Cells: Advancing Therapeutic Approaches for Cancer Treatment, *Cancers*, 2024, **16**, 2171, DOI: 10.3390/CANCERS16122171.

78 C. Lennicke, J. Rahn, R. Lichtenfels, L. A. Wessjohann and B. Seliger, Hydrogen peroxide - production, fate and role in redox signaling of tumor cells, *Cell Commun. Signal.*, 2015, **13**, 39, DOI: 10.1186/S12964-015-0118-6.

79 R. Ou, G. Aodeng and J. Ai, Advancements in the Application of the Fenton Reaction in the Cancer Microenvironment, *Pharmaceutics*, 2023, **15**, 2337, DOI: 10.3390/PHARMACEUTICS15092337.

80 C. Deng, Z. Ye, C. J. Zheng, H. Cheng and J. Ge, Iron-based nanozymes induced ferroptosis for tumor therapy, *Nanoscale*, 2025, **17**, 14103–14117, DOI: 10.1039/D5NR00880H.

81 S. Yu, H. Zhang, S. Zhang, M. Zhong and H. Fan, Ferrite Nanoparticles-Based Reactive Oxygen Species-Mediated Cancer Therapy, *Front. Chem.*, 2021, **9**, 651053, DOI: 10.3389/FCHEM.2021.651053/XML.

82 L. Feng, L. Feng, S. Gai, F. He, P. Yang and Y. Zhao, Multifunctional Bismuth Ferrite Nanocatalysts with Optical and Magnetic Functions for Ultrasound-Enhanced Tumor Theranostics, *ACS Nano*, 2020, **14**, 7245–7258, DOI: 10.1021/ACSNANO.0C02458.

83 Y. Wang, F. Gao, X. Li, G. Niu, Y. Yang, H. Li and Y. Jiang, Tumor microenvironment-responsive fenton nanocatalysts for intensified anticancer treatment, *J. Nanobiotechnol.*, 2022, **20**, 1–33, DOI: 10.1186/S12951-022-01278-Z.

84 B. Y. Ma, K. Yoshida, M. Baba, M. Nonaka, S. Matsumoto, N. Kawasaki, S. Asano and T. Kawasaki, The lectin Jacalin induces human B-lymphocyte apoptosis through glycosylation-dependent interaction with CD45, *Immunology*, 2009, **127**, 477–488, DOI: 10.1111/J.1365-2567.2008.02977.X.

85 A. E. Saunders and P. Johnson, Modulation of immune cell signalling by the leukocyte common tyrosine phosphatase, CD45, *Cell. Signal.*, 2010, **22**, 339–348, DOI: 10.1016/j.cellsig.2009.10.003.

86 D. G. T. Hesslein, R. Takaki, M. L. Hermiston, A. Weiss and L. L. Lanier, Dysregulation of signaling pathways in CD45-deficient NK cells leads to differentially regulated cytotoxicity and cytokine production, *Proc. Natl. Acad. Sci. U. S. A.*, 2006, **103**, 7012–7017, DOI: 10.1073/PNAS.0601851103.

87 B. D. Manning and A. Toker, AKT/PKB Signaling: Navigating the Network, *Cell*, 2017, **169**, 381–405, DOI: 10.1016/j.cell.2017.04.001.

88 A. S. Dhillon, S. Hagan, O. Rath and W. Kolch, MAP kinase signalling pathways in cancer, *Oncogene*, 2007, **26**, 3279–3290, DOI: 10.1038/SJ.ONC.1210421.

89 H. Yu, D. Pardoll and R. Jove, STATs in cancer inflammation and immunity: a leading role for STAT3, *Nat. Rev. Cancer*, 2009, **9**, 798–809, DOI: 10.1038/NRC2734.

90 P. J. Roberts and C. J. Der, Targeting the Raf-MEK-ERK mitogen-activated protein kinase cascade for the treatment of cancer, *Oncogene*, 2007, **26**, 3291–3310, DOI: 10.1038/SJ.ONC.1210422.

91 T. Kinoshita, T. Tada, S. Nakae, and I. Yoshida, Structural dissection of human mitogen-activated kinase ERK1, in *Worldwide Protein Data Bank*, 2009, DOI: 10.2210/PDB2ZOQ/PDB.

92 M. L. Hermiston, A. L. Tan, V. A. Gupta, R. Majeti and A. Weiss, The juxtamembrane wedge negatively regulates CD45 function in B cells, *Immunity*, 2005, **23**, 635–647, DOI: 10.1016/j.immuni.2005.11.001.

93 PTPRC - Receptor-type tyrosine-protein phosphatase C - Homo sapiens (Human)|UniProtKB|UniProt, https://www.uniprot.org/uniprotkb/P08575/entry, accessed on December 3, 2025.

94 T. Kinoshita, I. Yoshida, S. Nakae, K. Okita, M. Gouda, M. Matsubara, K. Yokota, H. Ishiguro and T. Tada, Crystal structure of human mono-phosphorylated ERK1 at Tyr204, *Biochem. Biophys. Res. Commun.*, 2008, **377**, 1123–1127, DOI: 10.1016/J.BBRC.2008.10.127.

95 U. Mauchle, G. T. Selvarajah, J. A. Mol, J. Kirpensteijn and M. H. Verheije, Identification of anti-proliferative kinase inhibitors as potential therapeutic agents to treat canine osteosarcoma, *Vet. J.*, 2015, **205**, 281–287, DOI: 10.1016/j.tvjl.2014.08.006.

96 K. E. Hevener, W. Zhao, D. M. Ball, K. Babaoglu, J. Qi, S. W. White and R. E. Lee, Validation of molecular docking programs for virtual screening against dihydropteroate synthase, *J. Chem. Inf. Model.*, 2009, **49**, 444–460, DOI: 10.1021/CI800293N.